NASA CR-159,307

NASA Contractor Report 159307

NASA-CR-159307
19800019924

Laboratory Evaluation of the Pointing Stability of the ASPS Vernier System

SPERRY FLIGHT SYSTEMS
PHOENIX, AZ 85036

CONTRACT NO. NAS1-15008
JUNE 1980

National Aeronautics and
Space Administration

Langley Research Center
Hampton, Virginia 23665

NASA Contractor Report 159307

Laboratory Evaluation of the Pointing Stability of the ASPS Vernier System

SPERRY FLIGHT SYSTEMS
PHOENIX, AZ 85036

CONTRACT NO. NAS1-15008
JUNE 1980

National Aeronautics and
Space Administration

Langley Research Center
Hampton, Virginia 23665

TABLE OF CONTENTS

LIST OF ILLUSTRATIONS

LIST OF ILLUSTRATIONS (cont)

LIST OF TABLES

LABORATORY EVALUATION OF THE POINTING STABILITY OF THE ASPS VERNIER SYSTEM

Brian J. Hamilton
Sperry Flight Systems

SUMMARY

The Annular Suspension and Pointing System (ASPS) is an end-mount experiment pointing system designed for use in the Space Shuttle. This report documents the results of the ASPS Vernier System (AVS) pointing stability tests conducted in a laboratory environment. A simulated zero-G suspension was used to support the test payload in the laboratory. The AVS and the suspension were modelled and incorporated into a simulation of the laboratory test. Error sources were identified and pointing stability sensitivities were determined via simulation. Statistical predictions of laboratory test performance were derived and compared to actual laboratory test results. The predicted mean pointing stability during simulated Shuttle disturbances was 1.22 arc seconds; the actual mean laboratory test pointing stability was 1.36 arc seconds. The successful prediction of laboratory test results provides increased confidence in the analytical understanding of the AVS magnetic bearing technology and allows confident prediction of in-flight performance. Computer simulations of ASPS, operating in the Shuttle disturbance environment, predict in-flight pointing stability errors less than 0.01 arc seconds.

SYMBOLS

PAYLOAD COORDINATES (See Figure 3)

X, Y, Z	Translation of Payload CG in Meters
θ, ϕ, ψ	Rotation of Payload About CG in Radians

MAGNETIC SUSPENSION (See Figure 3)

A, B, C	Axial Magnetic Bearing Stations
U, V	Radial Magnetic Bearing Stations
W	Roll Motor
$F_A \ldots F_W$	Force Applied by Each Station in Newtons
$\Delta g_A \ldots \Delta g_W$	Rotor Position in Each Magnetic Gap in Meters From Center

OTHER MISCELLANEOUS SYMBOLS

Z_o	Center of Mass Offset From Radial Force Plane in Meters
Keq	Effective Spring Constant at an MBA
π	PI
m	Mean of a Normal Distribution
σ	Standard Deviation of a Normal Distribution
σ^2	Variance of a Normal Distribution
R	Amplitude of a Pointing Disturbance in Arc Seconds
α	Direction of a Pointing Disturbance in Degrees (See Figure 28)
α_o	Direction (Like α) in Which Disturbance is Applied

INTRODUCTION

The Annular Suspension and Pointing System (ASPS) is an end-mount experiment pointing system designed for use in the Space Shuttle. The ASPS is composed of two major systems. The ASPS Gimbal System (AGS) provides coarse pointing using conventional dc torque motors to drive the gimbals. The ASPS Vernier System (AVS) provides high-resolution experiment pointing and isolation of the experiment from Shuttle disturbances, such as man-motion and Vernier Reaction Control System (VRCS) accelerations. The AVS uses a six-degree-of-freedom magnetic suspension to achieve experiment pointing stability of better than 0.01 arc seconds when operating in conjunction with the AGS in the Space Shuttle disturbance environment. At the occurrence of a Shuttle disturbance, the payload is allowed to translate in the soft suspension of the magnetic bearing gaps without disturbing the line-of-sight experiment pointing. Subsequently, rotations of the AGS gimbals are commanded to slowly recenter the magnetic gaps in preparation for the next perturbation. Thus, the payload becomes a constrained free flyer aboard the Space Shuttle.

The purpose of the tests described herein is to verify the feasibility of such an approach by measuring the pointing stability of actual protoflight hardware in the laboratory.

Background

Initial ASPS planning included a technology demonstration flight on an early Shuttle mission. Thus, a protoflight engineering model of the ASPS Vernier System (AVS) was fabricated for laboratory testing with the option of subsequent refurbishment for flight testing. As a result, the laboratory testing conducted during this program provides true credibility to the design since the AVS engineering model is full-size, protoflight-quality hardware.

The AVS Engineering Model (EM) test program consists of three phases: calibration, servo testing, and pointing stability testing. All test phases have been completed. The first two phases are documented in informal Sperry Flight Systems reports. The pointing stability tests are documented in this report.

The following technology deficiencies existed at the beginning of the pointing stability tests.

- Gap Sensing - The ASPS control laws require knowledge of the rotor (payload mounting platform) position within the magnetic gaps. Gaps are sensed at each magnetic bearing station via proximeters. These proximeters have a temperature sensitivity which make them unacceptable in the Shuttle thermal environment. The temperature sensitivity problem was discovered during the calibration test phase. In terms of system pointing stability, the sensitivity is approximately 0.5 arc second per degree centigrade. Control of the laboratory environment to ±0.25°C enabled continuation of the test program. Gap sensor improvement and alternate approaches are being designed in a parallel effort.

- Residual Hysteresis - The magnetic bearings and rotor are fabricated from a 50-percent nickel/steel alloy. This alloy was selected because of its inherently low flux hysteresis. Initial evaluation of the alloy showed no measurable hysteresis. However, the AVS engineering model proved to be a better measurement instrument for hysteresis. During the calibration test phase, low levels of residual flux were detected. The residual hysteresis results in an in-flight pointing error of approximately 0.5 arc second. This error was not visible during pointing stability tests due to the laboratory seismic noise environment. (This point is discussed later in this report.) The in-flight hysteresis error will be eliminated by improved heat treating of the nickel/steel alloy and ac compensation within the magnetic bearing driver electronics. The improved heat-treating processes have been defined and the electronic compensation is being designed in a parallel effort.

- Roll Torque - Potential payloads for ASPS have become larger; the largest current payload model has a mass of 7500 kg and inertias of 45,000 kg-m^2. While the torques produced by the gimbal motors and the forces produced by the magnetic bearings are adequate for such large payloads, the roll motor torque is deficient. This deficiency was discovered through analysis and simulation of the ASPS. Torque must be increased from 0.7 N/m to approximately 5.0 N/m. Roll torque can be increased by rescaling the roll motor design with attendant increases in rotor heating (local distortions) and radial disturbance torques. An alternate approach is being studied which uses magnetic bearings for production of roll torque. Knowing of the roll torque deficiency in advance, it was cost-effective to postpone testing of the roll degree of freedom. Testing of all five magnetic bearing degrees of freedom is discussed in this report; roll controls were inactive and roll freedom was passively constrained.

- Low Bias Mode - The dynamic range of magnetic bearing force is sufficiently large to require dual scaling through high and low bias modes. The need for a low bias mode was defined by analysis early in the ASPS design and prior to initiation of the laboratory test program. The low bias mode was not included in the EM hardware since it is a straightforward refinement of the basic technology. As discussed previously, the magnetic bearing drive electronics must be modified to compensate for residual hysteresis. The low bias mode will be added to the drive electronics during the same modification.

A primary objective of the pointing stability tests was to identify and quantify any additional technology deficiencies, thus providing a complete set of required technology improvements.

Test Philosophy

The flight performance of the ASPS must ultimately be predicted by analysis; flight pointing precision can never be demonstrated in the laboratory environment. Ground performance is drastically degraded by seismic noise, earth gravity, stray air currents, and the dynamic interaction between the AVS and the laboratory test setup (simulated zero-g suspension). Even so,

laboratory testing serves a necessary function in that it verifies technical understanding of the problem. Successful analytical prediction of the pointing performance of the AVS in the laboratory environment is a verification of the analytical tools used in making the prediction. Thus, confidence in the ability to predict in-flight pointing performance is gained from ground testing.

Toward this end, a computer simulation was assembled. The dynamics of both the AVS and the test setup were modelled. All significant error sources (AVS and test equipment) were identified and modelled. Using the simulation, pointing sensitivity to each error source was obtained. These sensitivities were combined statistically to predict the mean and deviation of the pointing error during laboratory tests. Hardware test results within a three-sigma target area are considered successful. All control system parameters were computed prior to initiation of laboratory tests. These computations, which are based on payload mass, inertia, and CM location data, were performed in a manner identical to that required to support a Shuttle mission. The control system parameters were not empirically adjusted during tests since the test objective was to hit the predicted target and not to obtain best-possible laboratory performance. Likewise, control bandwidths were set to values proposed for use on-orbit to maintain similarity between flight and laboratory systems.

Definitions

The following definitions are relevant:

- Pointing accuracy defines how close the experiment line-of-sight must initially point to the target. Since the primary error sources are mission- and payload-dependent (e.g. sensor bias and thermal distortions) and do not apply to the laboratory setup, accuracy was not tested.

- Pointing resolution defines the smallest amplitude command which the system will properly follow. This is a measure of the system's small-signal linearity; typical error sources are quantization and hysteresis. Resolution is measured in these tests.

- Pointing stability is divided into two areas: quiescent and dynamic.

- Quiescent stability defines how close the experiment line-of-sight must stay pointed to the initial point when no external disturbances are applied to the steady-state system. Quiescent stability values are expressed as 1σ.

- Dynamic stability, commonly referred to as VRCS stability, refers to the same system error, but in the presence of external disturbances. The colloquial name comes from the fact that an Orbiter VRCS jet firing is considered the worst-case external disturbance. Dynamic stability is considered to be a peak value above the 1σ quiescent value already discussed. (See Figure 1.)

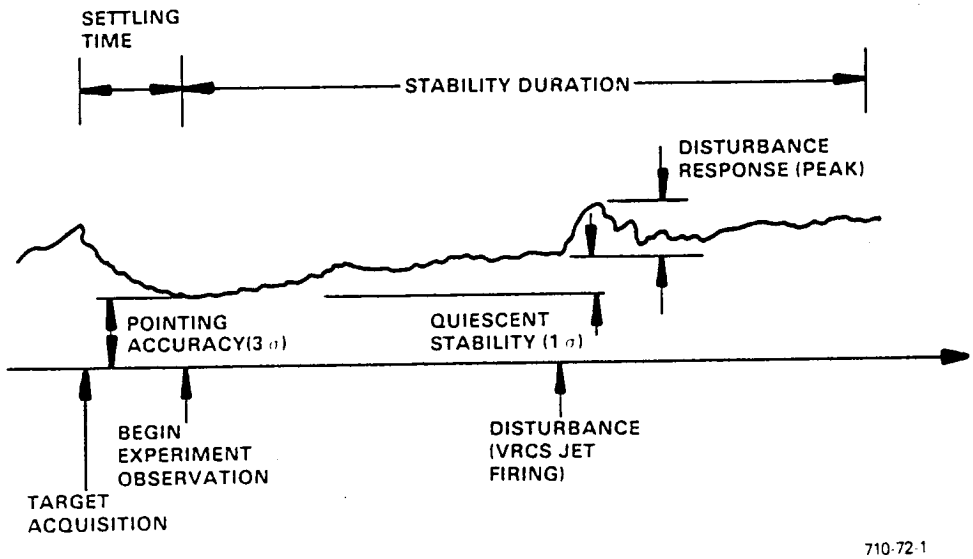

Figure 1
Definition of Stability

DESCRIPTION OF THE ENGINEERING MODEL TEST SETUP

The AVS engineering model is shown in Figure 2 with the payload mounting plate removed. It is a full-size working model of a flight AVS.

Definition of Variables

The AVS contains six magnetic actuators which operate against an L-shaped annular rotor providing six-degree-of-freedom control. Note that for all of the tests described herein, only a five degree-of-freedom suspension was used. The sixth degree, roll about the line-of-sight (Ψ), was passively constrained. Figure 3 defines the variable names used in this report. Note that three axial magnetic bearings, A, B, and C, combine to provide torques in the rotational axes θ and ϕ, and force in the translation axis Z. The two radial bearings U and V provide forces for translational control in the X-Y plane. No F_W was applied in these tests. Each of the magnetic actuators contains an integral position sensor capable of measuring the rotor position at that point, and the outputs of these sensors are referred to as Δg_A ... Δg_V where zero is gap center and the polarities are the same as shown for the bearing forces in Figure 3.

Basic Control System

The implementation of the engineering model includes drive electronics for the bearings which take force commands as inputs, and sensor electronics which output the Δg signals. The position control loops are then closed through an AD/4 analog computer (Figure 4). The partitioning is made so that the AD/4 contains all functions which will ultimately reside in flight software. A patch diagram of the AD/4 electronics is shown in Figure 5. Note that the servo compensation has the same structure for all six degrees of freedom, being proportional plus integral plus lead/lag. This is a very significant point since the controllers intended for use in space incorporate a rate damping term which analysis has shown will improve performance nearly an order of magnitude. In flight, rate information is available from a three-axis gyro package. Since this inertial reference unit or other sensor of sufficient resolution was not available for these laboratory tests, lead/lag was used instead of the superior rate damping compensation. Note the CG offset decoupling terms also in Figure 5. These will be referred to often since they represent one of the most significant error sources in dynamic stability performance. These terms, when properly set, decouple the translational controllers from the pointing axes by effectively applying the radial forces U and V at the payload center of mass instead of the base.

Hardware

Figure 6 depicts the laboratory test setup in a block diagram/cartoon format. Figure 7 shows the actual engineering model test hardware. The 216-kilogram dummy payload is suspended in roughly zero-G as described below.

- Axial freedom - Figures 8 and 9 show the counterbalance beam from which both the dummy payload and an equal 216-kilogram counterweight are suspended.

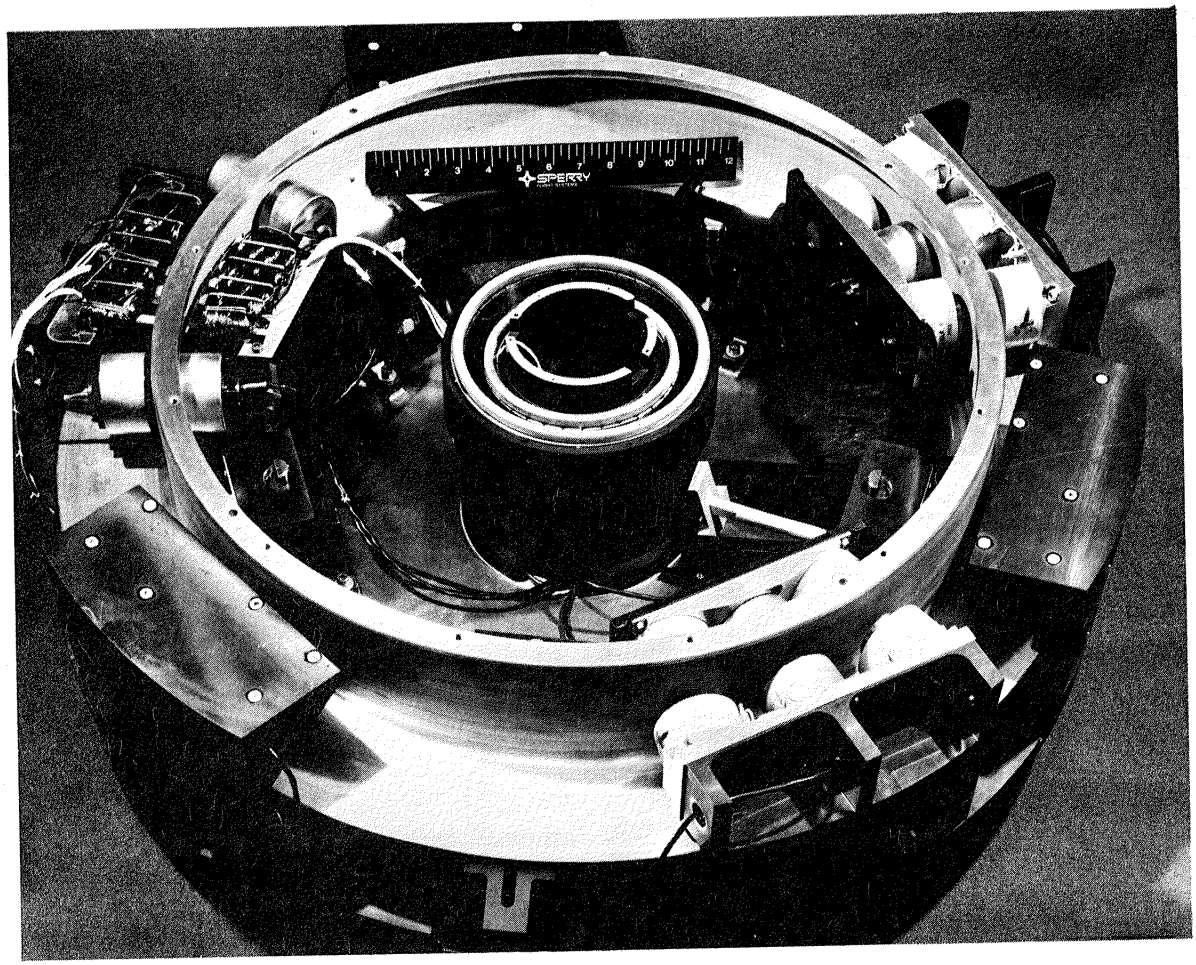

3-13066-3

Figure 2
AVS Engineering Model With Top Plate Removed

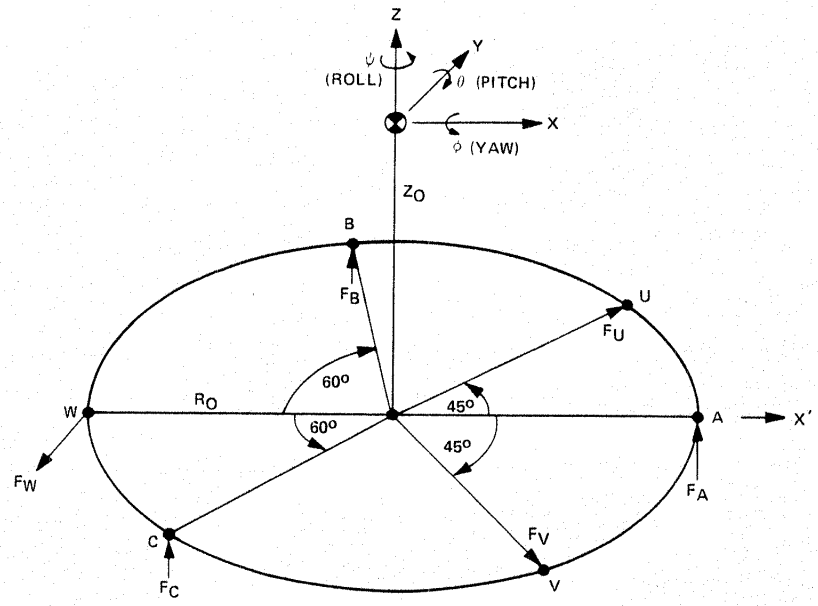

$F_X = F_U \cos 45^o + F_V \cos 45^o$

$F_Y = F_U \sin 45^o - F_V \sin 45^o - F_W$

$F_Z = F_A + F_B + F_C$

$T\phi = F_B R_O \sin 60^o - F_C R_O \sin 60^o + F_U Z_O \sin 45^o - F_V Z_O \sin 45^o - F_W Z_O$

$T\theta = -F_A R_O + F_B R_O \cos 60^o + F_C R_O \cos 60^o - F_U Z_O \cos 45^o - F_V Z_O \cos 45^o$

$T\psi = F_W R_O$

46-5110-20-13-78-R1

Figure 3
Vernier Actuator Forces and Moments

Figure 4
AVS Electronics

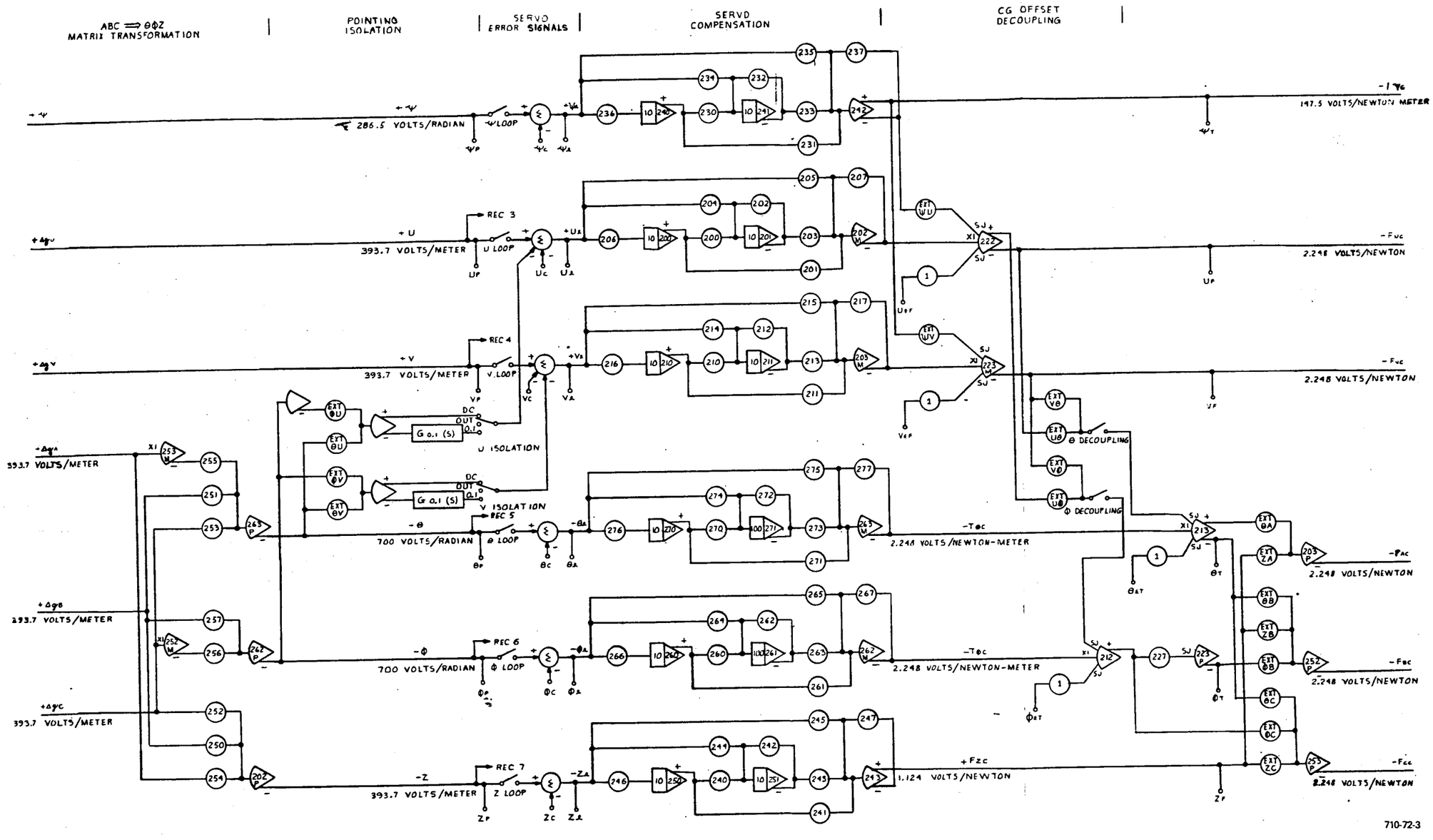

Figure 5
AD/4 Patch Diagram

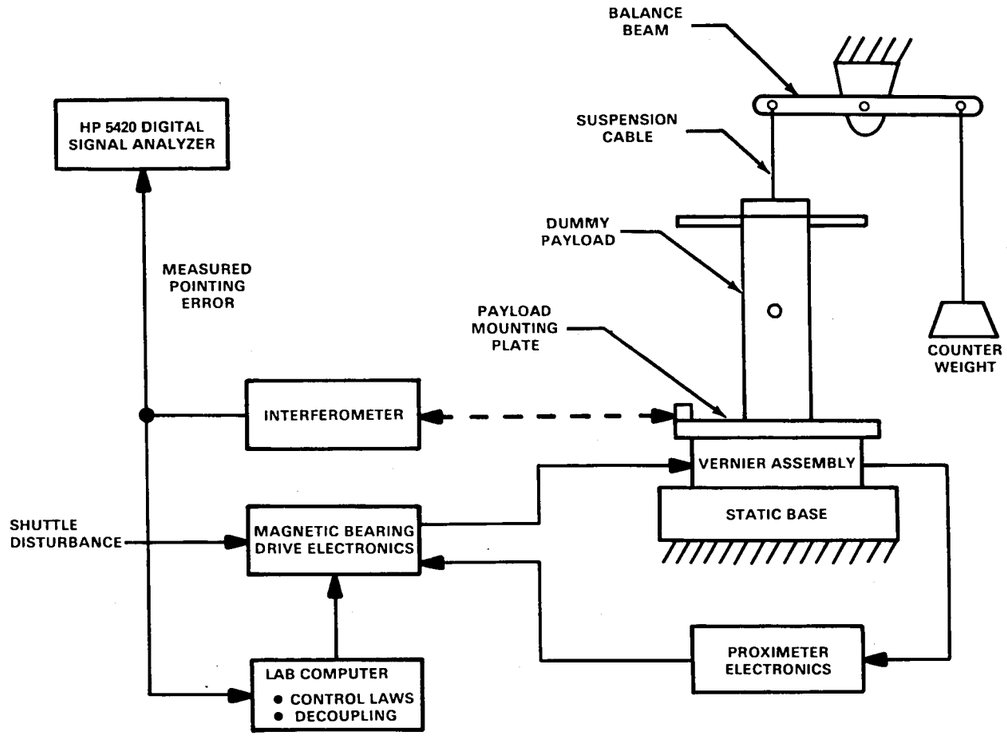

Figure 6
Laboratory Test Setup

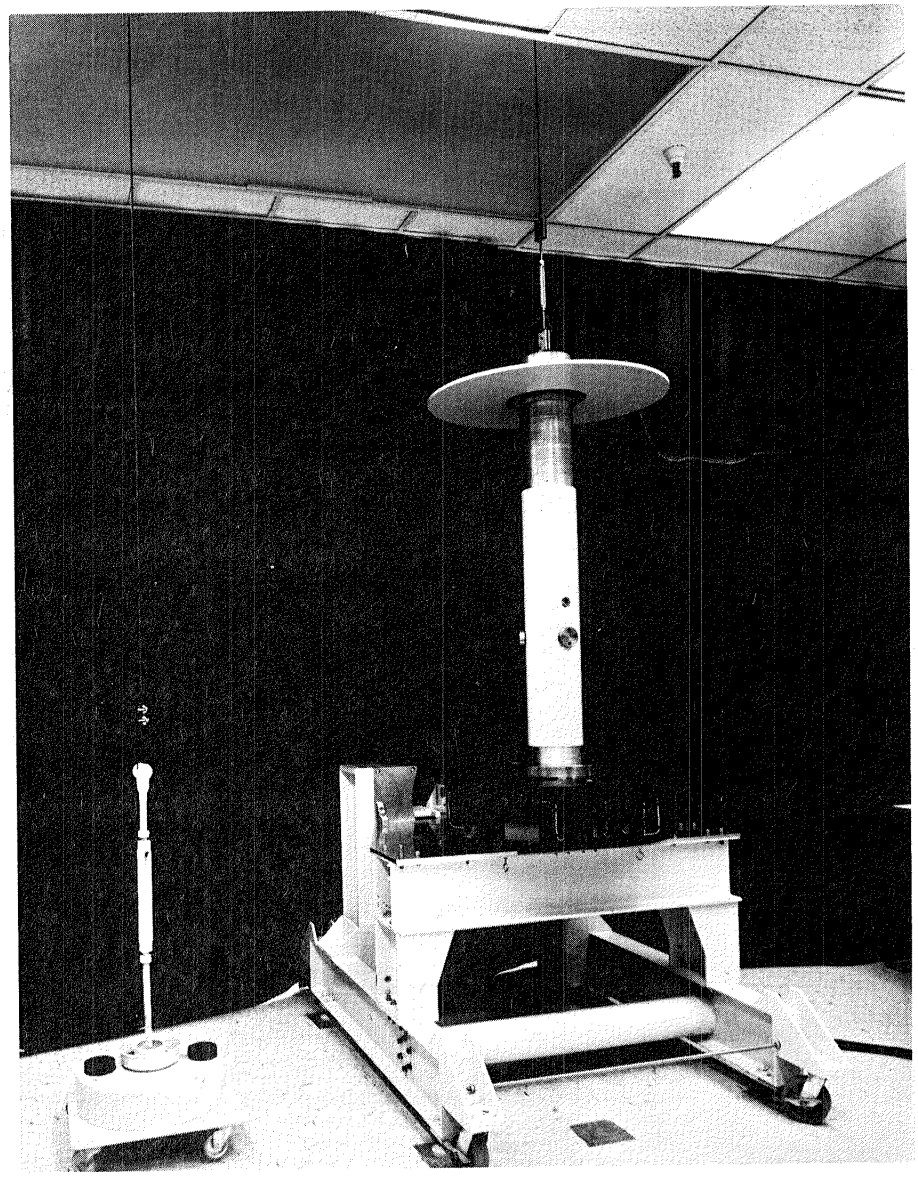

9-13680-3

Figure 7
AVS With Suspended Dummy Payload

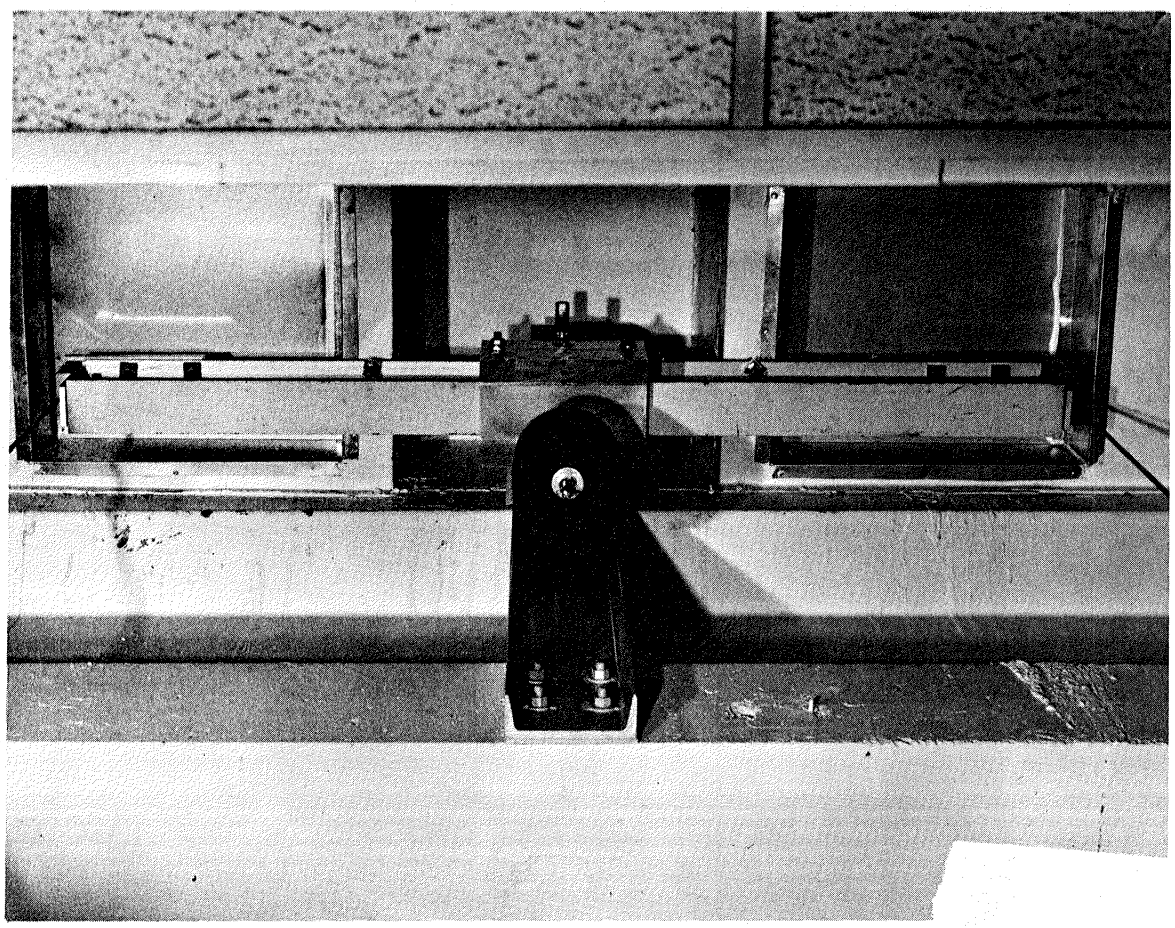

9-13680-2

Figure 8
Balance Beam Assembly

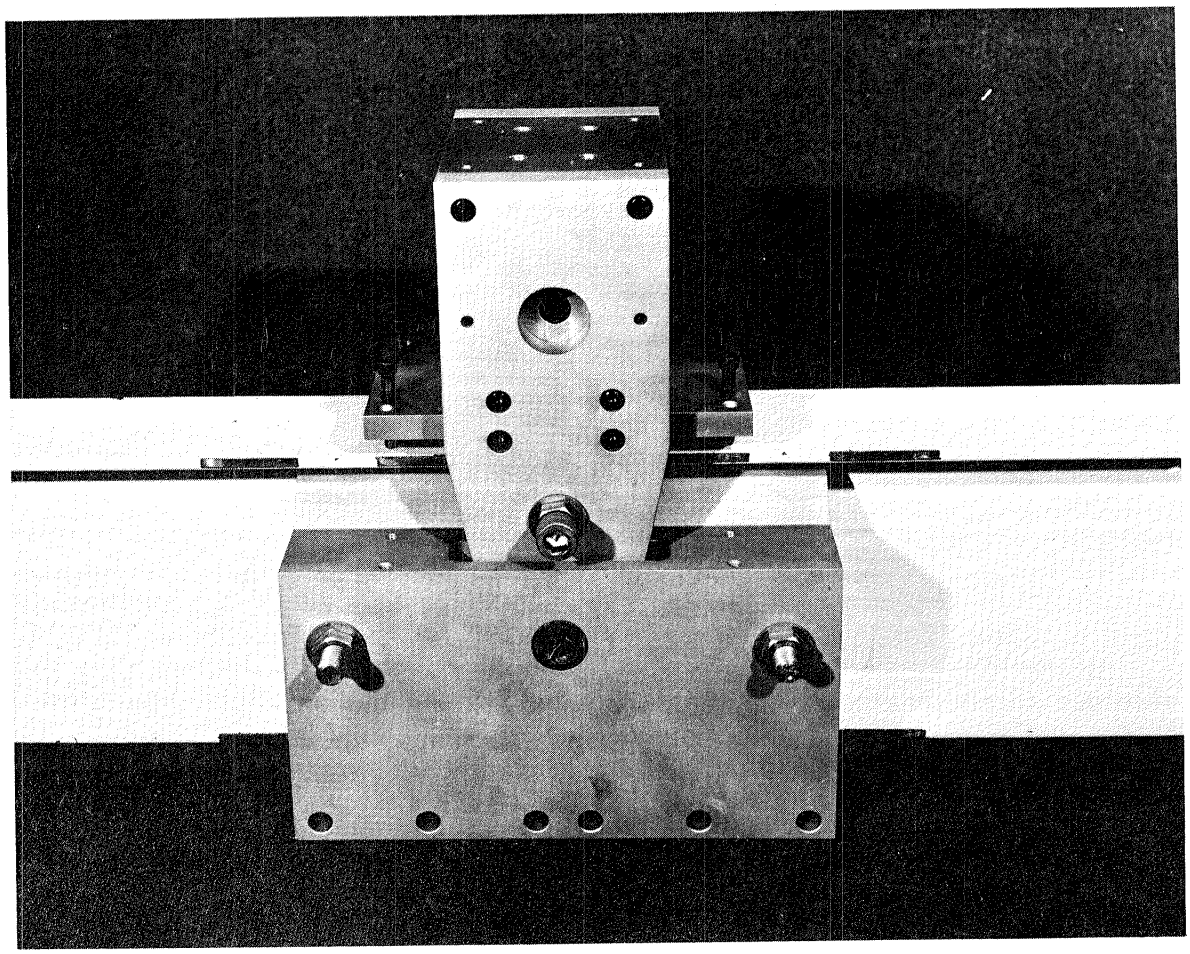

3-13593-1

Figure 9
Balance Beam Pivot Assembly

The pivot spring constant of the balance beam can be adjusted to nearly zero, resulting in a good zero-G simulation.

- Pointing freedom - Figures 10 and 11 show the pivot assembly which attaches the suspension cable to the payload. This assembly allows free rotation in both pointing axes, and is positioned so that the pivot axes intersect at the payload center of mass. This results in neutral stability.

- Radial freedom - The radial axes are not ideal like the others, but are sufficient for test purposes. They are characterized as a pendulum or positive radial spring of approximately 0.6 N/mm. The resultant natural frequency is approximately 0.25 Hz.

With the payload suspended in this way, it is possible to test the system in a one-G environment, despite the fact that each magnetic bearing is capable of supporting less than 10 pounds.

HP5526A Laser Interferometer

In order to measure the pointing angles θ and ϕ with sufficient resolution, a laser interferometer was set up as shown in Figure 12. This setup can resolve the angle between rotor and stator to better than 0.001 arc second. Digital-to-analog converters then provide an output signal which can be used either for recording or as a loop feedback signal from an independent sensor. (See Figure 6.)

HP5420A Digital Signal Analyzer

In the laboratory environment there is a significant amount of quiescent noise due to motions of floor, ceiling, and air. Since this noise is of greater amplitude than the VRCS disturbance response and of similar frequency content, normal noise reduction and filtering techniques do not apply. In a case such as this, it is necessary to use synchronous averaging, a technique easily implemented by the HP5420A Digital Signal Analyzer. By repeating the VRCS transient many times and averaging the results (Figures 13 and 14), the random element in the signal can be greatly reduced with no degradation in the actual signal content as would be the case if filtering techniques were employed. In general, the improvement in signal-to-noise ratio obtained from this technique is proportional to the square root of the number of independent averages taken.

Laboratory-Related Error Sources

The engineering model test setup simulates, as closely as possible, the conditions of an on-orbit AVS pointing a typical (mass, inertias, CM offset) payload in 5 degrees of freedom. Several differences do, however, exist between the laboratory and space environments, and these should be mentioned. First, rate damping is not being used in the laboratory. Second, the laboratory seismic noise environment may effect some system nonlinearities such as hysteresis. Third, the stator is fixed in the laboratory, and a radial pendulum exists on the payload. Imperfections in the suspension pivots may

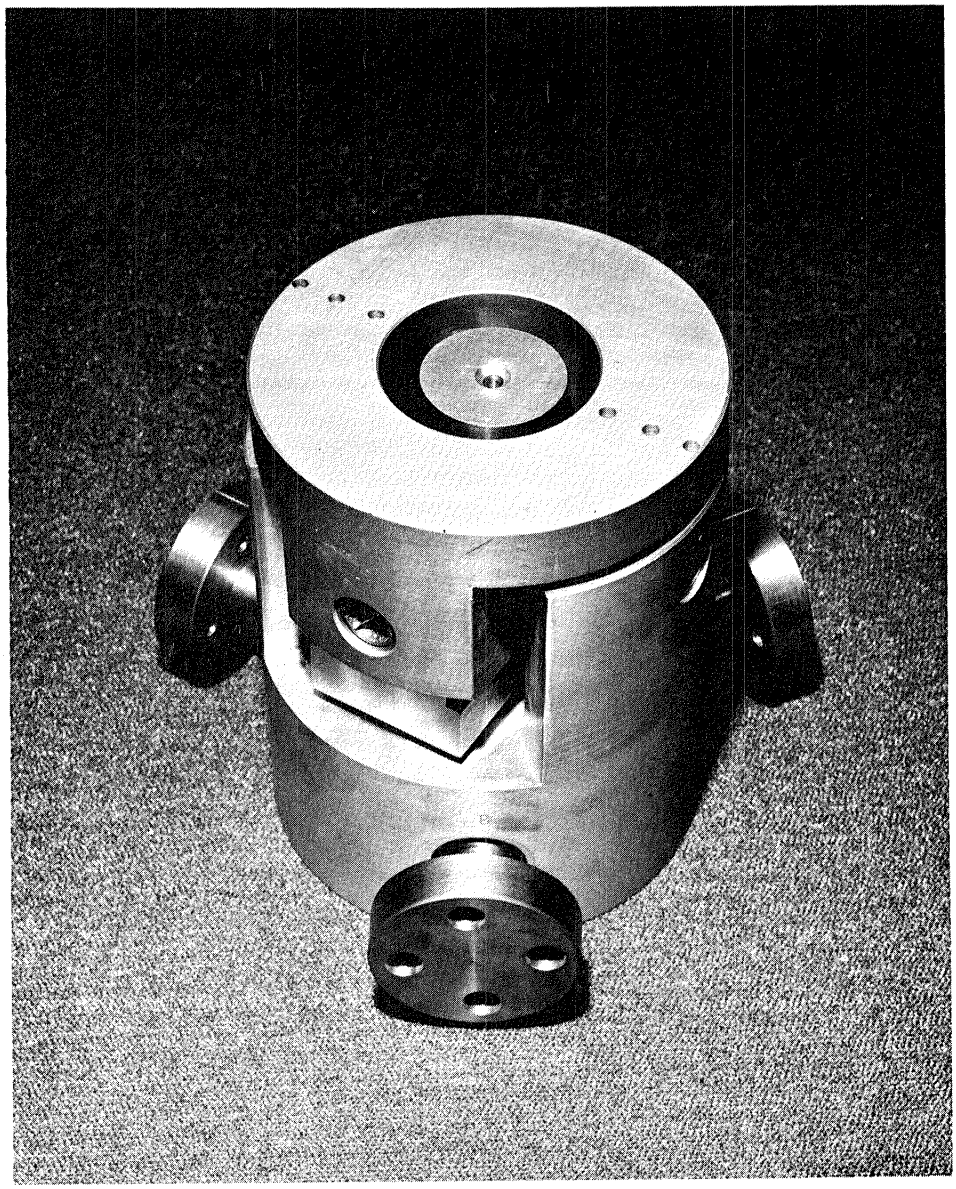

14-13551-3

Figure 10
Payload Pivot Assembly

cause nonideal zero-G conditions. Laboratory temperature is controlled to ±0.25°C and is therefore not a significant error source. Likewise, support electronics and operating personnel are located in a separate control room to minimize air currents within the test area. (See Figure 4.)

All of these factors will cause the laboratory data to differ from that which would be expected in space, some helping and some hindering. Every effort has been made to accurately account for these differences in the testing and simulation so that extrapolations to the expected space performance can be made.

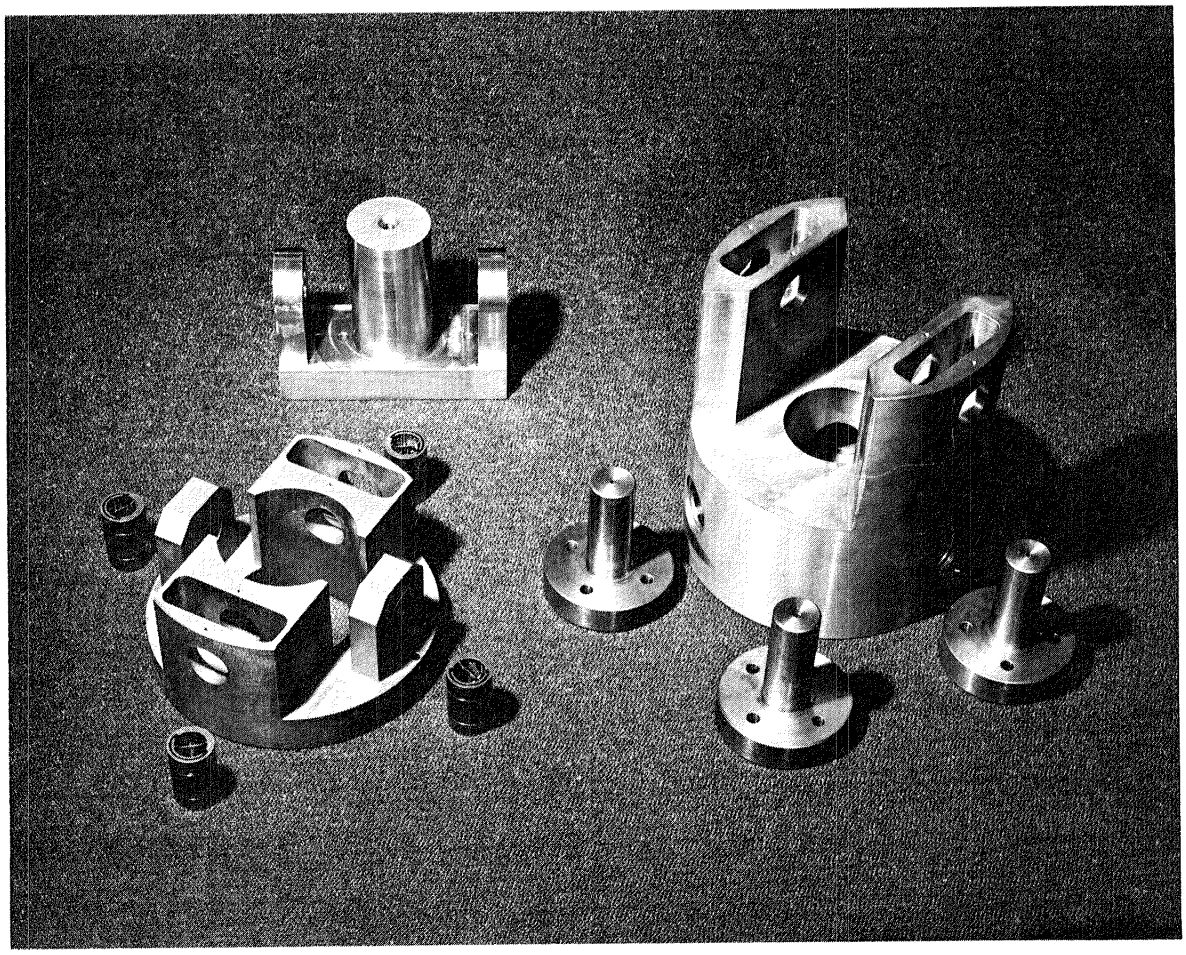

14-13551-2

Figure 11
Payload Pivot, Exploded View

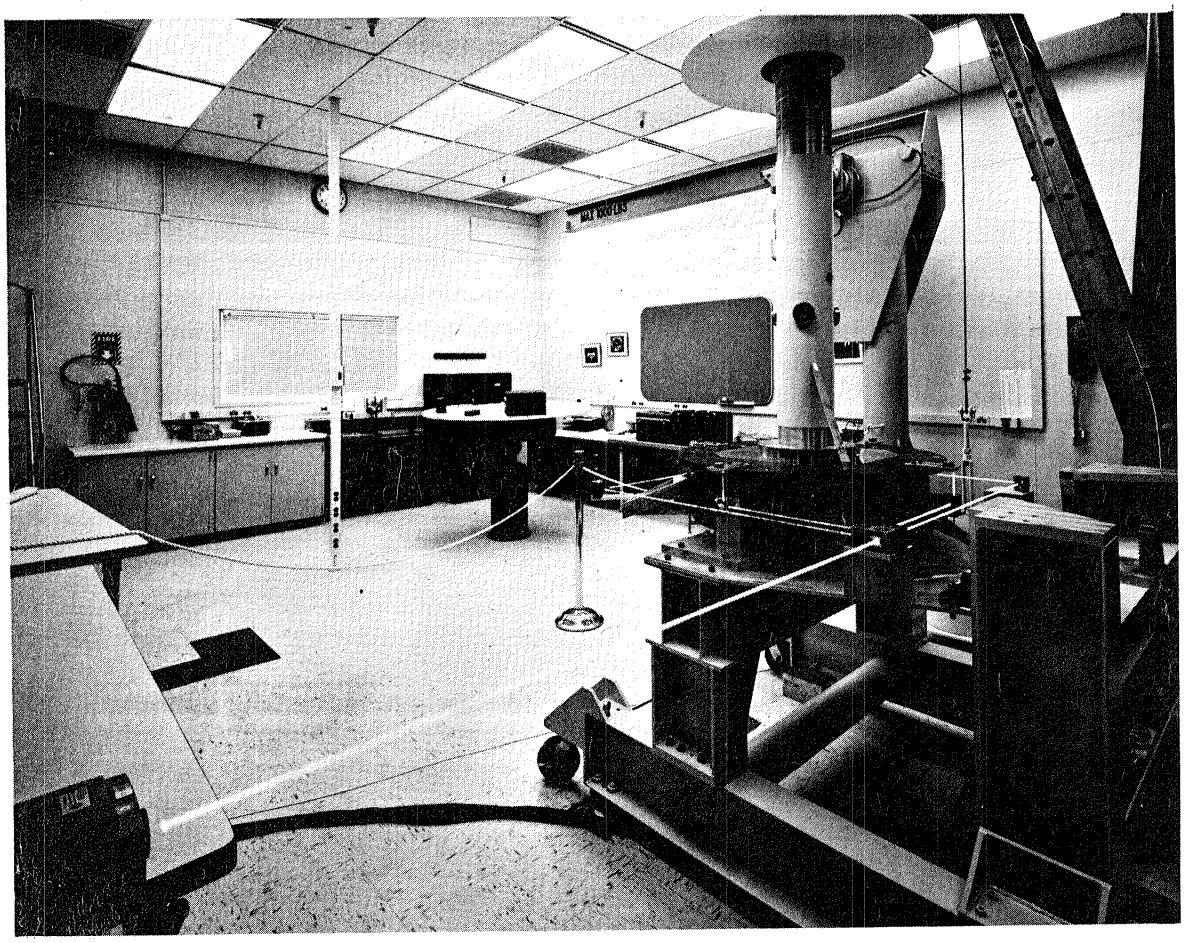

12-13782-1

Figure 12
Laser Measurement of θ and ϕ

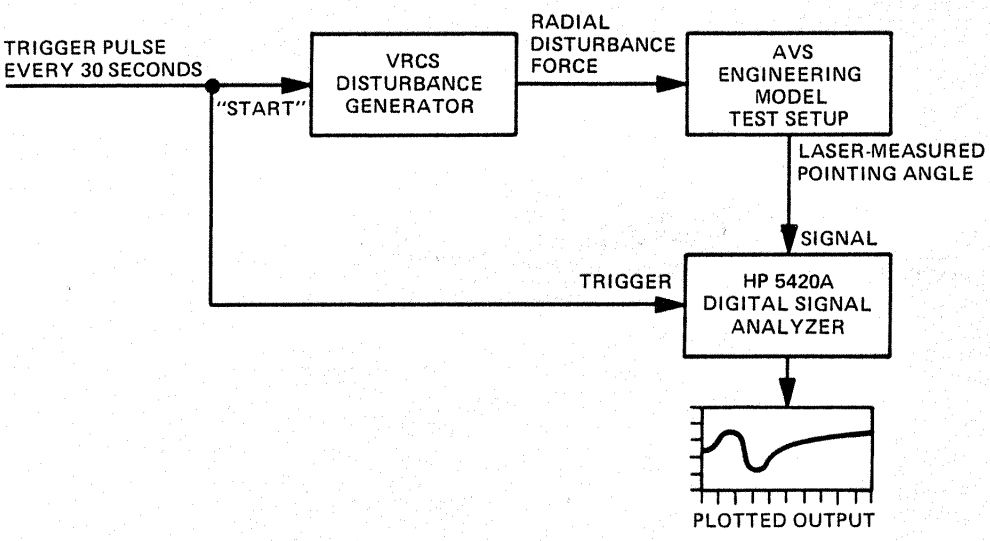

Figure 13
Synchronous Averaging

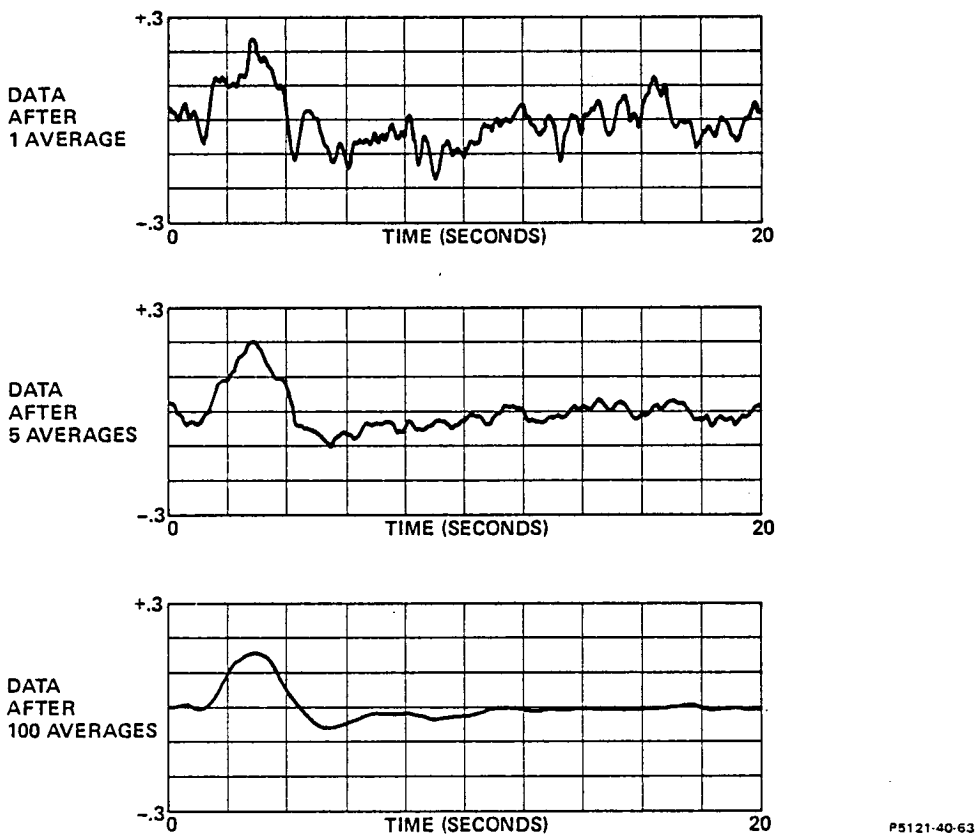

Figure 14
Effect of Synchronous Averaging on Data With Random Noise

TEST RESULTS

System Linearity

Small-signal nonlinearities impact pointing performance. Command resolution tests can be made to define small-signal nonlinearities. Tests show that the resolution is better than laboratory measurement capability; therefore, clean pointing maneuvers can be demonstrated at the lower limit of the laboratory instrumentation. Figure 15(a) shows a triangle wave of 0.02 arc second peak commanded to the ϕ axis while no command is applied to θ. For this test it was necessary to use 3-hertz bandwidth pointing loops and synchronous averaging to reduce background noise to an acceptable level. Figure 15(b) shows the same test using a square wave command.

Based on previous test results, hysteresis nonlinearity had been expected. Several techniques were used to try to find it and measure its severity, but the system performed as though no hysteresis were present. An example of this is shown in Figure 16. Disturbances are applied to the system, similar to the VRCS stability tests, but in two different ways. First, the same disturbance is applied repeatedly and averaged, then the disturbance is alternated, positive and negative, and averaged. If hysteresis were present, the responses should differ since the alternating case would minimize the residual buildup. As can be seen in Figure 16(c), there is virtually no difference. An explanation is given in the next section.

Quiescent Stability

Linearity tests showed no measurable small-signal nonlinearities in the system. This is surprising when two sources of error, hysteresis and PROM-lookup quantization, are known to exist in the laboratory test setup. It is theorized that the reason for this discrepancy is the presence of seismic noise in the laboratory environment. The engineering model stator is suspended from the floor of the laboratory, and the payload is suspended from the ceiling. Since both floor and ceiling are in motion, both inertially and differentially, a large amount of quiescent noise is to be expected, and, in fact, exists. The HP5420 Digital Signal Analyzer can be used to remove this noise from the data, but it must be remembered that the hardware itself is undergoing continuous random motion due to external disturbances. The amplitude of this motion is a function of the suspension bandwidths of the system. With 1-hertz bandwidth pointing loops, over 1 arc second of peak-to-peak pointing motion exists in the absence of deliberate disturbances.

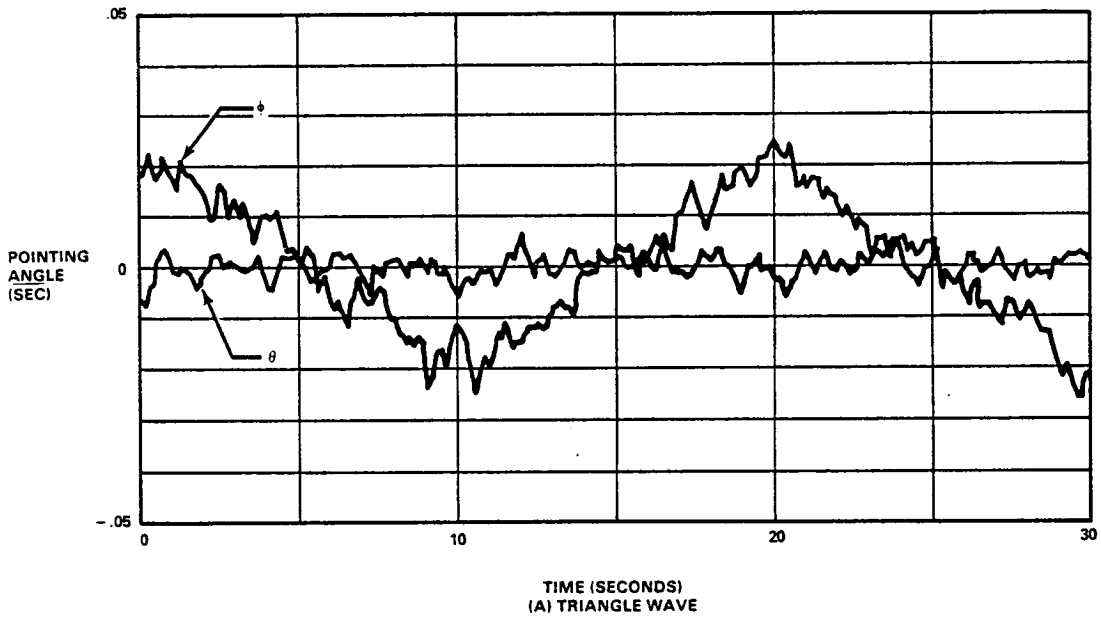

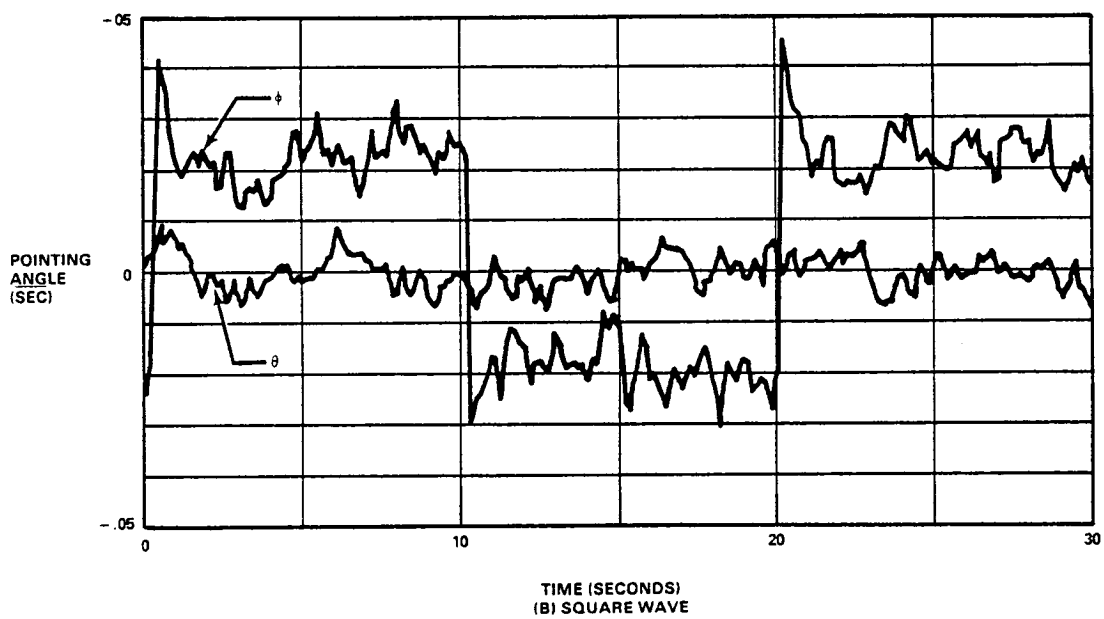

Figure 15
Command Resolution Data

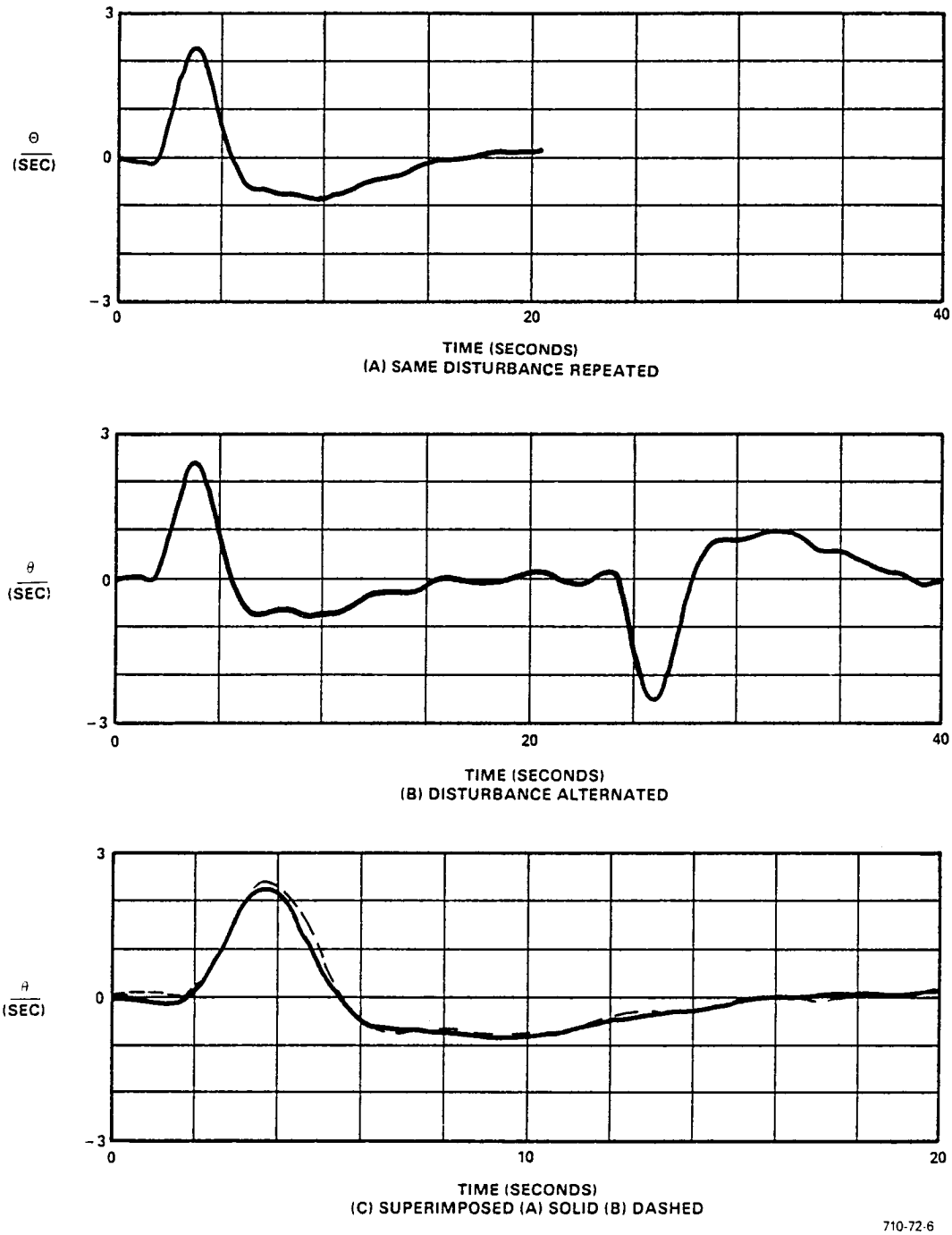

Figure 16
Hysteresis Data

When it is considered that one least-significant bit of PROM lookup output corresponds to 0.2 arc second of pointing, two things are clear. First, the quantization is large enough to be visible; but secondly, the quiescent noise is causing random crossings of several least-significant bits all the time, resulting in a sort of interpolation between the discrete values of the PROM bank outputs.

Furthermore, it is plausible to assume that the same quiescent noise acts as a superimposed ac degaussing signal effectively negating the presence of hysteresis.

However, the question of whether the quiescent noise is, in fact, the result of the quantization must still be addressed. To determine the effects of quantization, the PROMs were removed from the system, leaving only the raw proximeter outputs. While these signals are nonlinear and seriously degrade the MBA calibrations, they are continuous. Thus with the PROMs removed, there are no sources of quantization in the entire AVS system. (The laboratory test setup is all analog.) Figure 17 shows the quiescent motion of θ and ϕ viewed by the interferometer with the PROMs both in and out. Note that there is little to no difference between these two cases; thus PROM lookup quantization is not a significant contributor to the total quiescent noise. It is therefore concluded that the noise is primarily seismic in nature.

Dynamic Stability

Description of the VRCS Disturbance. - As mentioned previously, the worst-case external disturbance to the system during fine pointing is the firing of a thruster by the Shuttle Vernier Reaction Control System (VRCS). This Orbiter subsystem controls the spacecraft's attitude in three axes using reaction jets located in the tail. As a result of their location, they cause translational accelerations as well as rotation as tabulated in Figure 18. These data form the basis of disturbance models which have been used in previous simulation studies at Sperry Flight Systems, NASA, and JPL. Previous studies have concluded, based on payload bay constraints, Orbiter CG location, etc, that the AVS is most affected by the VRCS when a pitch disturbance is introduced at low-elevation gimbal angles, i.e. near the horizontal caged position. For this ASPS orientation, the Orbiter translation component of the pitch disturbance is in the radial plane of motion for the AVS, and to prevent contacting hard stops, a pure radial translation force must be applied to the payload. This action requires maximum use of the decoupling control law since a pure translation force requires application of forces directly at the payload center of mass. (The ASPS is an end-mount pointing system.)

The block diagram of Figure 19 describes the disturbance as it occurs in space. The jet force (translation component) is applied to the Orbiter mass, and the Orbiter begins to accelerate away from the payload, thus increasing the gap. This gap error is applied to a 0.1-hertz bandwidth radial centering servo which, in turn, commands a radial force to return the payload to the center of the gap. If the decoupling does, in fact, provide this radial force directly at the payload CG, the payload will catch the Shuttle which is moving away from it, and zero the radial gap error without applying an overturning moment to the payload, i.e. without introducing pointing error.

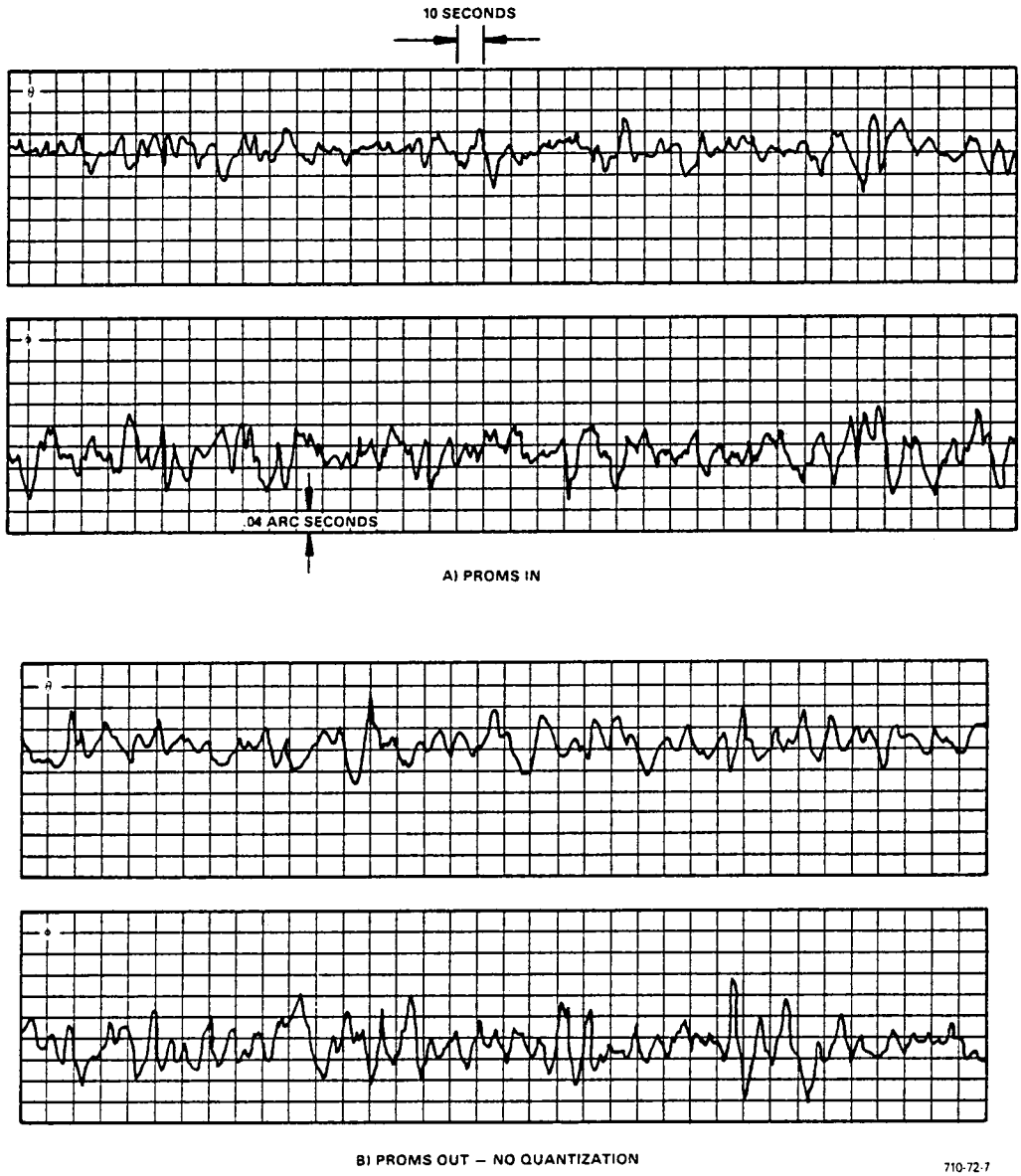

Figure 17
Quiescent Noise

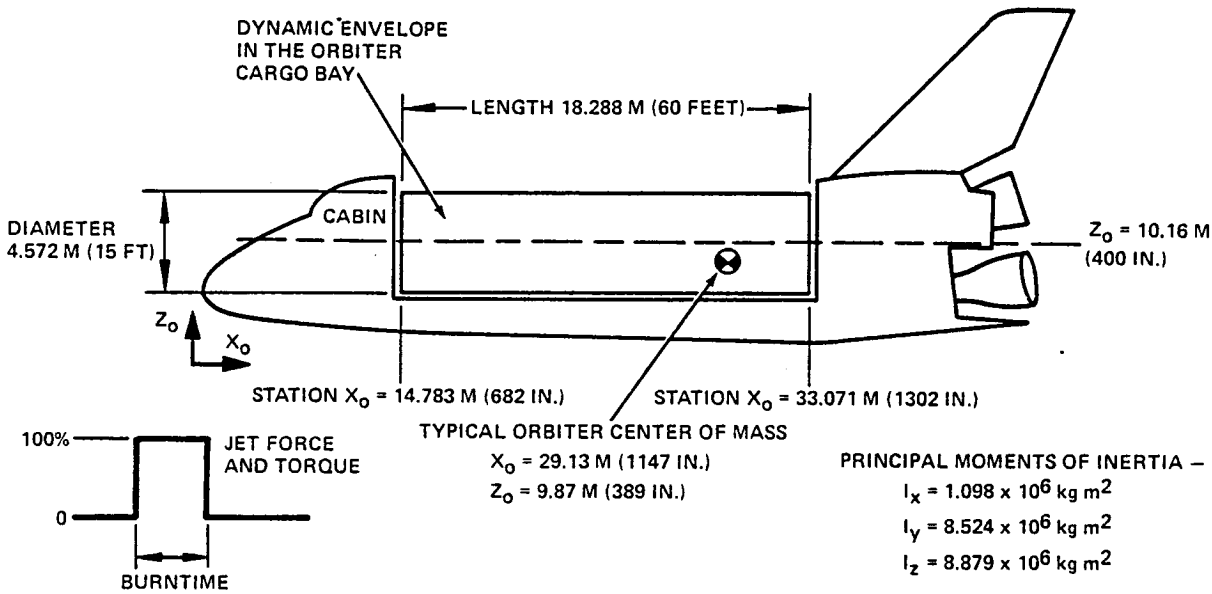

VRCS AXIS	BURN TIME (SEC)	PEAK FORCES AND TORQUES					
		F_x (N)	F_y (N)	F_z (N)	T_x (N-m)	T_y (N-m)	T_z (N-m)
ROLL	.200	0	-184.0	196.0	682.4	0	0
PITCH	.520	0	0	222.4	0	-2487.5	0
YAW	.480	0	38.2	84.9	0	0	2592.6

MASS = 84,562 kg

P5121-40-59

Figure 18
Orbiter VRCS System

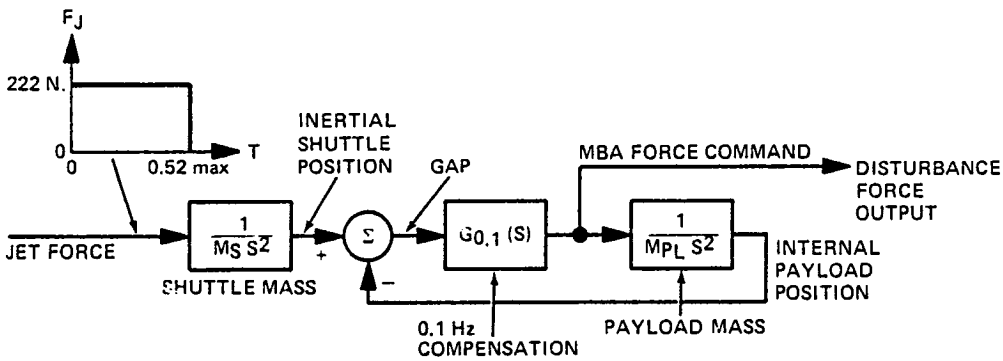

P5121-40-60

Figure 19
VRCS Disturbance Generator Block Diagram

In order to duplicate this transient in the laboratory, a "black box" has been built which implements the block diagram of Figure 19. The force command signal from the compensation block is extracted and becomes the output in response to a trigger input which fires the jet. This output is the force which will actually be required of the radial bearings during a worst-case disturbance, so the signal is simply applied directly to the bearings in the laboratory. What is being tested is the vernier system's ability to apply that worst-case force to the payload center of mass.

Note that the actual motion of the payload will bear little resemblance to that which would occur in space. This is because the return spring of the radial pendulum in the laboratory will prevent the payload from achieving the final velocity it would in space. However, since the laboratory stator is not really moving away, this situation is desirable and allows the entire transient to occur in the laboratory without touching a hard stop. In fact, it is not possible to duplicate the time profiles of both force and gap without actually allowing large-scale motion of both rotor and stator in the laboratory test setup. This would be impractical. Fortunately, only the force profile is significant to decoupling errors, and the gap motion does not matter. Ideally, the additional force being applied to the system by the radial pendulum is applied at the payload CG, and no pointing error will result.

Sensitivity Study and Prediction. - The above section describes a means whereby the VRCS transient can be studied in the laboratory. Forces will be applied exactly as they would be in space and the payload pointing angles θ and ϕ will be measured to determine how much the payload overturns during the transient. The question to be asked at this point is, "How much pointing error is too much?" The 0.01-arc second on-orbit specification should not apply in the laboratory where many extraneous error sources exist and the low bias mode bearings have not been implemented. To determine what constitutes acceptable results, a simulation which included all sources of error due to the laboratory environment, in addition to the vernier itself, would be needed. Such a simulation could then be subjected to the same VRCS transient as the hardware, and sensitivities to the various errors could be studied.

A nonlinear digital simulation like the one described above has, in fact, been written. The remainder of this section describes the use of this simulation to support the laboratory tests.

Error Sources: The first step in predicting system performance is the identification of error sources. All known sources must be considered, whether due to the AVS itself or to the special test equipment peculiar to the laboratory. For purposes of analysis, these error sources can be grouped into categories as shown below:

Type 1: Errors Proportional to Force

Errors in this category include:

- Decoupling matrix
- Force transformation matrix

- CG offset uncertainty
- Arm lengths (torques)
- MBA errors proportional to force command.

Type 1 errors result in VRCS pointing errors early in the transient because the resultant error torques occur immediately upon application of translational forces, even before any motion has occurred.

Type 2: Errors Proportional to Gap

Errors in this category include:

- MBA errors proportional to gap
- Rotor position sensor errors (proximeters)
- System Test Equipment (STE) pivot spring constants
- CG offset from pivot (STE)

Type 2 errors do not result in error torques to the pointing axes until after translational motion has begun; thus they become more significant later in the transient than do the cumulative effect of Type 1 errors.

As a result of the time shift between these two types of errors, it must be recognized that they do not exactly cancel or add together when errors of both types exist simultaneously. Figures 20 and 21 show normalized time responses for the two types of errors. Note that Type 1 errors cause a disturbance earlier than do Type 2 errors. If the two errors shown were applied simultaneously with opposite polarities, a curve like that of Figure 22 would result. Note that even though the normalized peak amplitude of both disturbances, separately, was 1, they do not cancel one another completely due to their shapes. However, since the peaks do coincide, the peak errors are additive as illustrated in Figure 23. This latter property will be useful in prediction of system performance, but the fact remains that errors of Types 1 and 2 must be nulled separately for optimum performance.

Type 3: Asymmetric Errors

In a multi-degree-of-freedom system like the AVS, torques are typically the result of a sum of forces which individually originate in separate actuators or matrix elements. Ideally, all these individual paths are identical, but in practice, the errors which exist in the system will vary from one actuator to the next, or one degree of freedom to the next. As a result of these variations within specified tolerances, one should expect a different net error if forces or motions exist in one plane than if they exist in another. This lack of symmetry about the payload line of sight is characteristic of Type 3 errors. It should be clear that Type 3 errors can result from variations in either Type 1 of 2 described above.

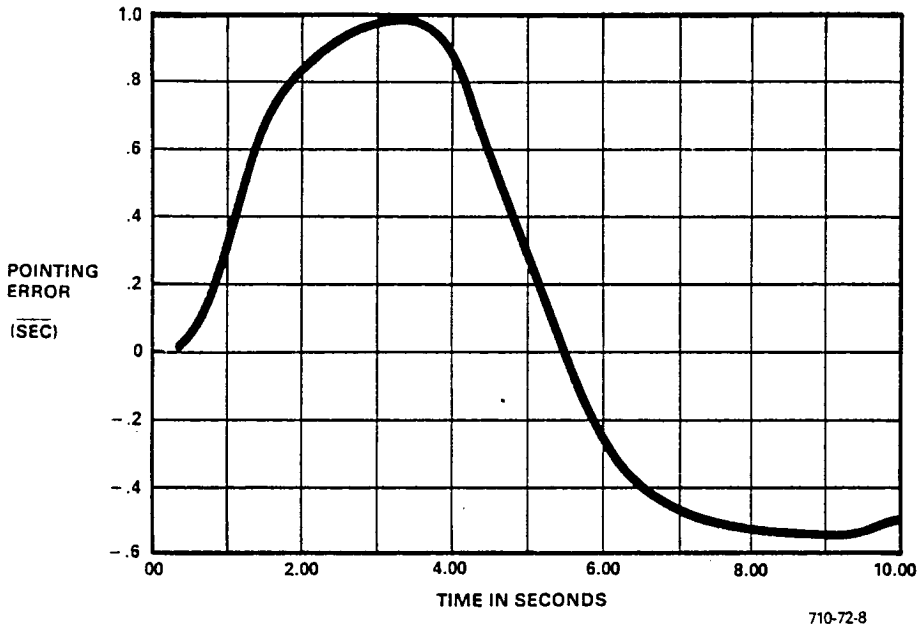

Figure 20
Normalized Response to Type 1 Errors

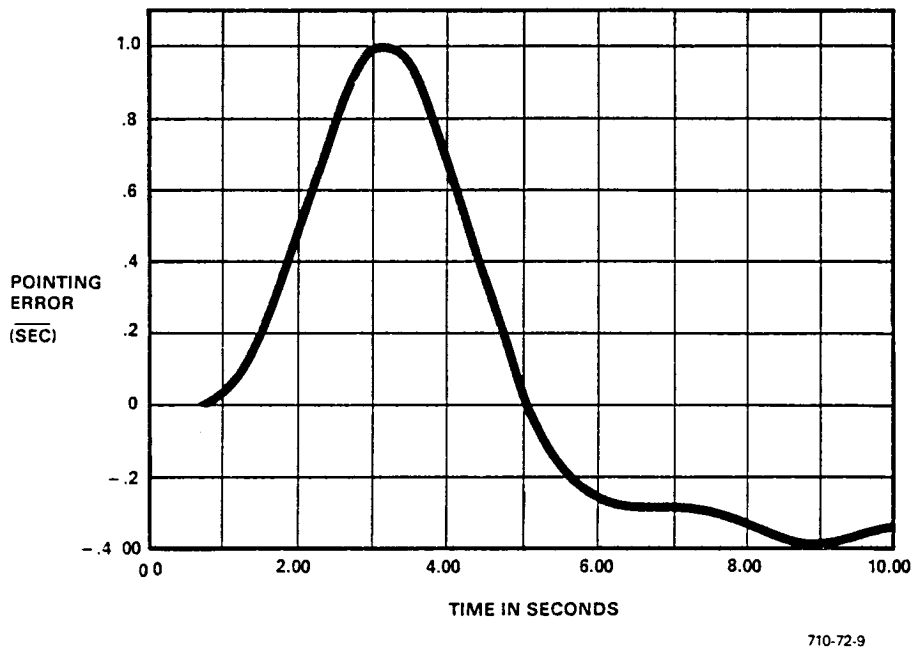

Figure 21
Normalized Response to Type 2 Errors

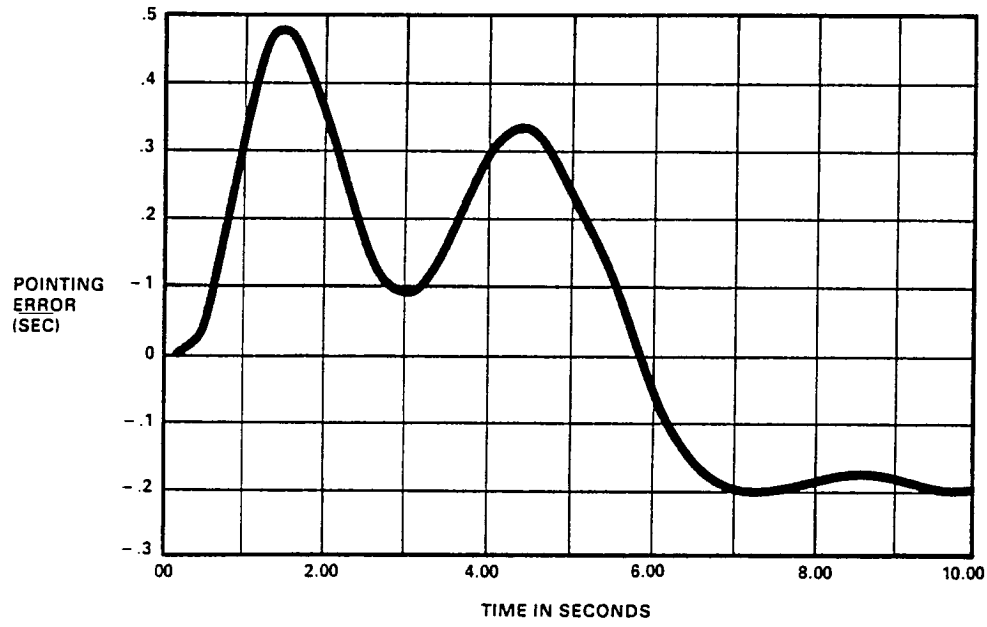

Figure 22
Cancellation of Type 1 and 2 Errors

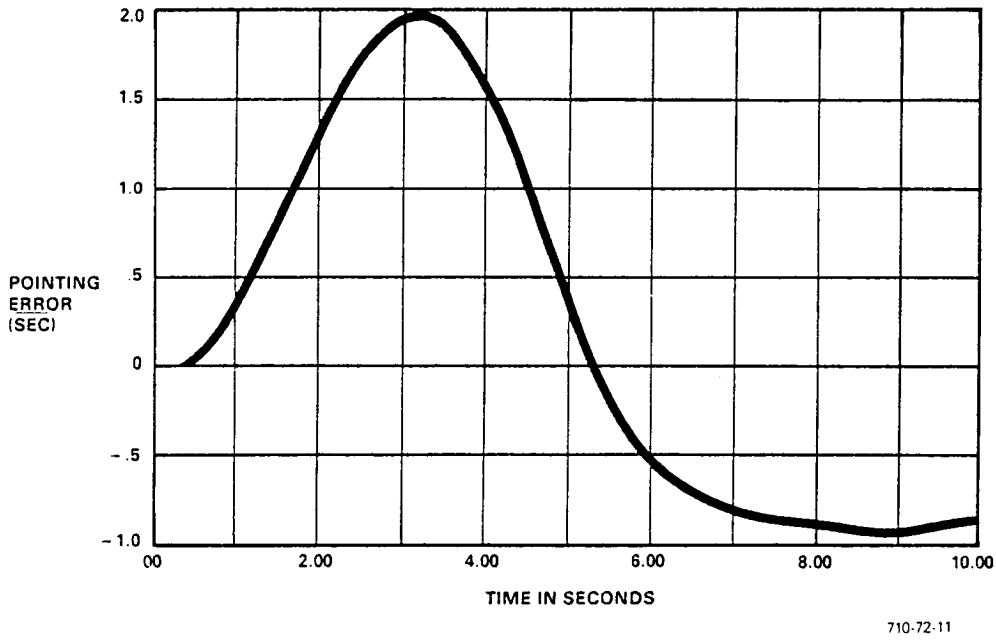

Figure 23
Addition of Type 1 and 2 Errors

Sensitivities and Tolerances: While all errors in both types (1 and 2) cause peak errors at about the same time, the errors are not equal. The system performance may prove to be much more sensitive to one error than to another, even in the same group. For this reason, it is necessary to determine the sensitivity of system performance to a known perturbation (i.e. 1 percent) in each error. This can be done in the simulation by simply varying each parameter 1 percent, in turn, and observing the results of the VRCS transient. Each error source has been studied in this manner, and the results are described below, beginning with the least significant.

In each case, a pure θ-axis disturbance is being considered, thus removing several matrix elements from significance. It is anticipated that a similar result could be derived at any angle of disturbance due to system symmetry. Pointing bandwidth is 1 Hz.

- Axial MBA Arm Lengths - These are the arms through which the axial forces cause pointing torques. Mechanical tolerance stackups result in a 0.5-percent (3σ) tolerance on these arms. As expected, θ motion is four times more sensitive to arm A than to arms B or C. For 1-percent variations, θ errors are:

  A - 0.104 arc second

  B - 0.026 arc second

  C - 0.026 arc second

- Force Transformation Matrix - Three elements of this matrix break the θ torque into A, B, and C force commands. Again, θ motion is four times more sensitive to the A element than to the B or C. The tolerance on all matrix elements (AD/4 pots) has been set at 0.6 percent (3σ). θ errors due to 1-percent variations in each element are:

  θA - 0.104 arc second

  θB - 0.026 arc second

  θC - 0.026 arc second

- Decoupling Matrix - Two elements of this matrix command θ decoupling torques as a result of U or V force commands. The tolerance is 0.6 percent (3σ). θ errors due to 1-percent variations are:

  Uθ - 0.078 arc second

  Uϕ - 0.078 arc second

- MBA Force Gains - Scale factor errors in MBA force proportional to force commands can be up to 1 percent (3σ) since the specification for the bearings is 1 percent of full-scale force over the range.

  A - 0.104 arc second

  B - 0.026 arc second

  C - 0.026 arc second

  U - 0.078 arc second

  V - 0.078 arc second

- CG Offset Uncertainty - The location of the payload center of mass has been calculated to a tolerance of ±1.5 percent (3σ). The error due to a 1-percent variation is 0.156 arc second.

- STE Pivot Spring Constant - The pivot assembly, at the point where the payload meets the suspension cable, may be nonideal. A spring constant would cause an error torque when the cable angle changed during radial translation. (Thus it is a Type 2 error.) While every attempt has been made to minimize this spring, engineering judgement says that some should remain. This spring is virtually impossible to measure, independent of other similar error sources, so an estimate has been made of 20 N-m/rad (3σ). This estimate is based on previous experience with similar designs. Sensitivity is 0.015 arc second per N-m/rad.

- CG Offset from Pivot - As a result of the uncertainty of CG position, it is possible to have the CG not coincident with the pivot axes. This presents a Type 2 error totally unrelated to the decoupling error mentioned previously. The origin of this additional error is the fact that the cable tension vector no longer acts directly on the center of mass, but instead acts through an arm. Whenever the pivot angle is nonzero, the lateral component of cable tension results in an error torque. Because the cable tension is quite large, this is a very sensitive error, resulting in 0.239 arc seconds of error for a 1 percent CG offset from pivot. As mentioned previously, the CG uncertainty is ±1.5 percent (3σ).

- MBA Errors Proportional to Gap - Since there are two independent variables in a magnetic bearing force characteristic (force command, gap), gradients with respect to each must be considered. When force errors proportional to gap (Type 2) exist, the effect is that of an equivalent spring, either positive or negative, depending on the gradient. The maximum tolerable slope which remains within the calibration specification of 1 percent is

$$\frac{(.01)\ F_{max}}{G_{max}} = 25.5 \text{ N/m (radial bearing)} \qquad (1)$$

Therefore a 3σ limit on this error is 25.5 N/m. Sensitivity to such a spring is 0.019 arc second per N/m for both U and V. It should be noted that only the radial bearings are considered since axial gap motion is very small during this transient.

Limits of ± 25.5 N/m (3σ) come from the calibration specification and assume that the mean, or most likely error, is zero. In fact, these spring constants have been measured in the laboratory as shown in Figures 24 and 25. Since actual data exist, they will be used for the prediction. The measured spring constants were 9 N/m (U-axis) and 55 N/m (V-axis). The Appendix derives estimates for the mean and standard deviation of 32 and 16.3, respectively. Clearly, the V-bearing is out of specification so these values are necessary if the prediction is to be plausible. This becomes especially true in view of the strong sensitivity to this error.

- Rotor Position Sensor Errors - These gap-sensing errors are inherently a part of other errors presented above.

Prediction of System Performance: All significant error sources have been defined; the system's sensitivity to each is known; and tolerances on their values have been estimated or specified. With this information, it should be possible to predict the way in which the system will perform. Classically, this would be done by the methods of worst-case analysis, in which each parameter is simultaneously set to its most extreme value in such a polarity that all errors add together. While this technique is correct, it would be very unlikely that such a situation could ever exist. The worst-case analysis places an upper bound on the error, but what we are interested in is the probability density of errors below the bound. A good prediction for laboratory performance would be the error most likely to occur, statistically, even if that error is well below the worst-case result.

Such a statistical analysis is reasonably straightforward for these data due to two helpful facts. First, the variations of each parameter are, in fact, statistically independent of each other. They are due to resistor tolerances, mechanical stackups, calibration errors, etc., which have no interactions between parameters. Secondly, as can be seen in Figures 20 through 23, the effects of the various errors will add together reasonably well at the peak value regardless of their types (1 or 2). When these conditions exist, the Central Limit Theorem can be invoked and a table such as Table 1 can be made in which the mean and standard deviation of system error (peak) due to each parameter is listed and then combined into a single mean and variance as follows:

$$m = \sum_{i=1}^{n} m_i \tag{2}$$

$$\sigma^2 = \sum_{i=1}^{n} \sigma_i^2 \tag{3}$$

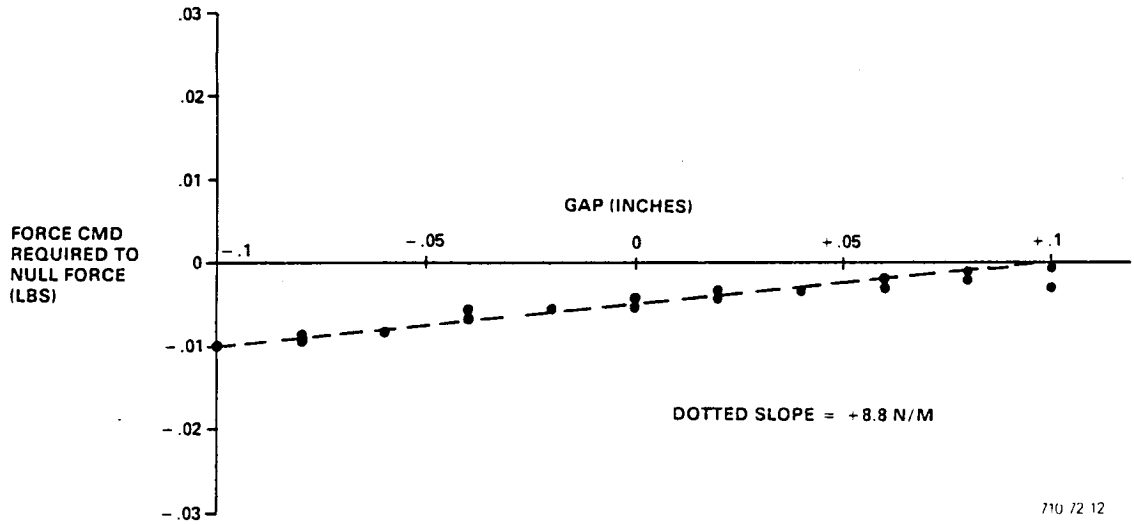

Figure 24
U-axis Spring Constant

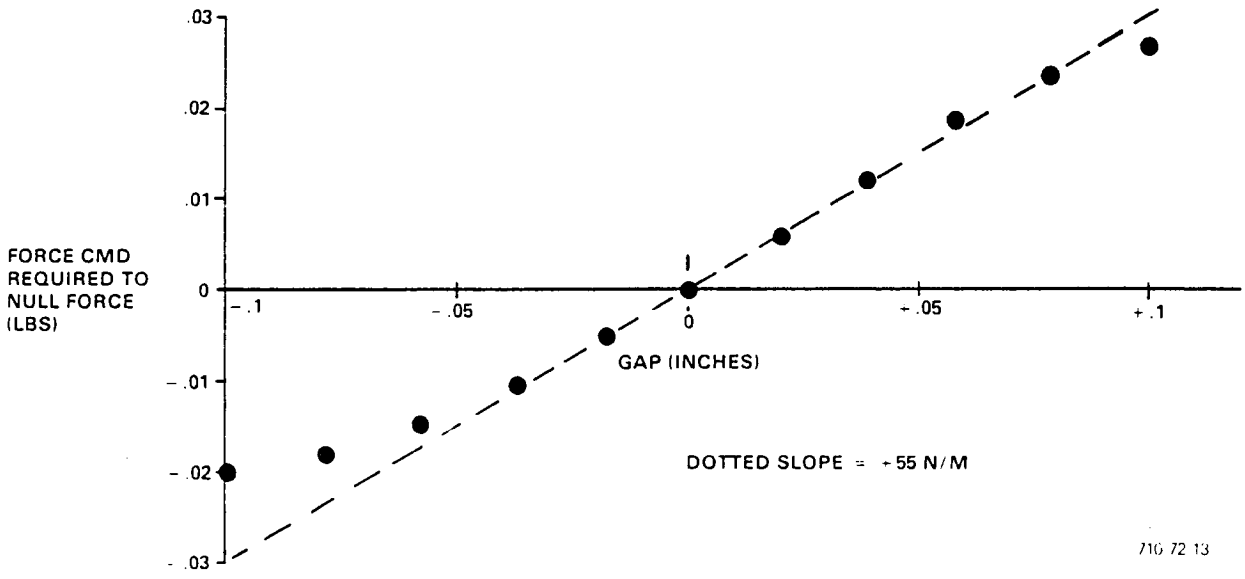

Figure 25
V-axis Spring Constant

TABLE 1

ERROR SENSITIVITIES

Error Source	Sensitivity (arc second) (To a 1 percent perturbation, or as noted below)	Tolerance (In percent or as noted)		Net Error ($\overline{sec}$)	
		Mean	σ	Mean	σ
Axial MBA Arm Lengths A	.104	0	.167	0	.0174
B	.026	0	.167	0	.0043
C	.026	0	.167	0	.0043
Matrix, Torque → Force θA	.104	0	.2	0	.0208
θB	.026	0	.2	0	.0052
θC	.026	0	.2	0	.0052
Matrix, Decoupling θU	.078	0	.2	0	.1560
θV	.078	0	.2	0	.1560
MBA Force Gains A	.104	0	.333	0	.0347
B	.026	0	.333	0	.0087
C	.026	0	.333	0	.0087
U	.078	0	.333	0	.0260
V	.078	0	.333	0	.0260
STE Pivot Spring	.015 per N-m/rad	0	6.66 N-m/rad	0	.1000
CG Offset From Pivot	.239	0	.5	0	.1195
MBA Gap Errors	.019 per N/m	32 N/m	16.3 N/m	.61	.3097
	.019 per N/m	32 N/m	16.3 N/m	.61	.3097
				1.216	.518 = 1σ

These two numbers represent a performance prediction by defining the pointing error due to the VRCS transient to be a random variable which is approximately normally distributed and has approximate mean and variance as above. The probability density function for this random variable

$$f(x) = \frac{1}{\sqrt{2\pi}\sigma} e^{-(x-m)2/2\sigma2} \qquad (4)$$

is plotted in Figure 26, and interpreted as follows: the probability that the pointing error lies between two values, a and b, is numerically equal to the area under the curve f(x) between the lines x = a and x = b.

As an example, the following statement can be made. There is a probability of 0.989 that the total pointing error due to a VRCS disturbance in the laboratory will lie between 0.0 arc second and 2.77 arc seconds under the conditions assumed for this analysis.

Radial VRCS Disturbance Data. - VRCS force disturbances were applied to the AVS engineering model. A very large body of data was taken on this subject over a period of five months which spans a variety of configurations, bandwidths, and special test cases. For complete coverage of these data, the reader is referred to the laboratory notebooks being kept for this program identified as ASPS/EM, Volumes 4 and 5. To stay within the scope of this report, only one data set will be presented. This data set, taken during the last week of December 1979, embodies the most careful and complete set of data ever taken on the AVS/EM radial VRCS performance. Each piece of data is the result of 100 independent averages on the HP5420 analyzer under optimum laboratory conditions. Absolutely no attempt has been made to empirically alter any control system parameter; thus, this data represents the baseline AVS performance in the face of the errors tabulated in Table 1.

The data set is presented in Figure 27, where the synchronously-filtered, laser-based measurements of θ and ϕ in response to VRCS disturbances in a variety of radial planes are plotted. Pointing bandwidths of 1 Hz apply throughout. At this point the disturbance angle, alpha, is defined to describe the direction in which the radial disturbance is applied. As an aid, assume for the moment that all decoupling is removed. Referring to Figure 3, it is clear that if the rotor is pushed inward at station A, a positive θ disturbance will result. This direction of radial force input, and the resulting rotation, are defined to have an alpha of 0 degree. Thus the angle, alpha, can describe both the input direction and the resulting payload rotation axis. For planar motion, these two would, of course, be equal. If a pure negative force in the U-axis is applied, the alpha would be +45 degrees, since U is 45 degrees away from bearing A. The resultant +45-degree payload rotation would consist of equal amounts of $+\theta$ and $-\phi$ disturbance. Summarizing, Figure 28 shows a view down on the payload plate from the payload CG and the alpha values for points on the perimeter. A VRCS disturbance force at alpha degrees consists of pushing inward on the rotor at that point on the perimeter. A disturbance angle of rotation of alpha degrees results from a disturbance force of alpha degrees in the absence of decoupling.

It should be clear, after this exercise of defining disturbance angles, that the measured rotations in the θ and ϕ axes must be combined to obtain the actual magnitude of the disturbance which occurred in the plane of the disturbance. In Figure 29, the peak values reached by each curve in Figure 27 are tabulated; then the true peak amplitude of the disturbance is derived using the relationship:

$$\text{peak amplitude, } R = \sqrt{\theta^2_{peak} + \phi^2_{peak}} \qquad (5)$$

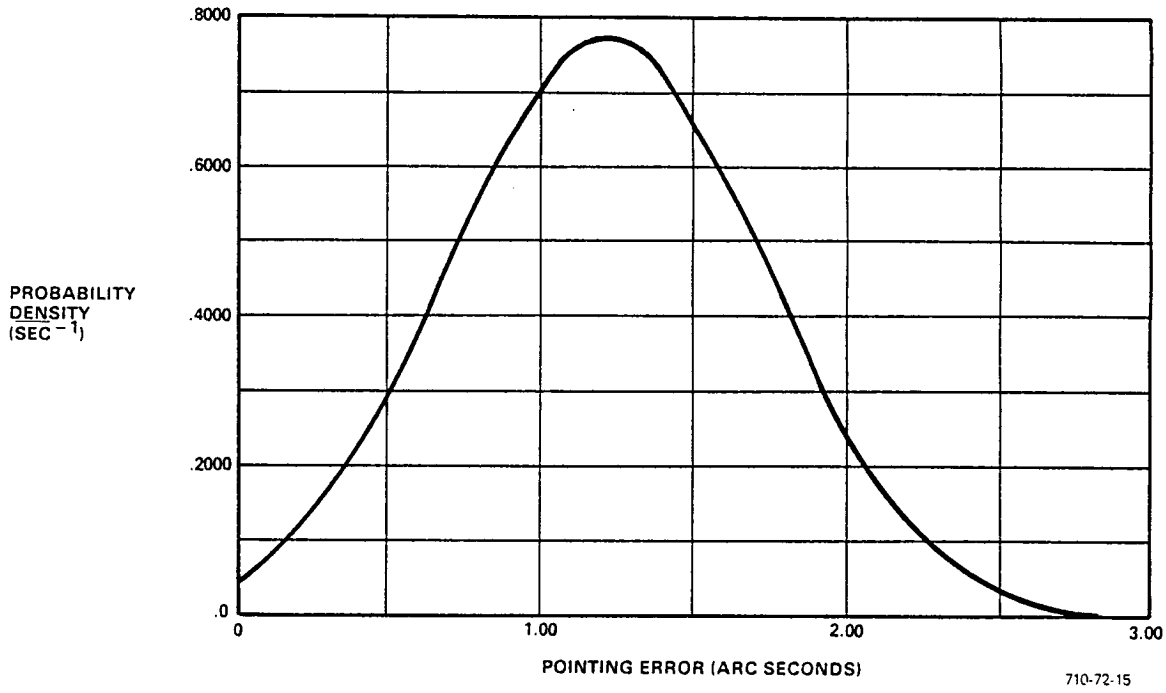

Figure 26
Predicted Probability Density Function of Pointing Error

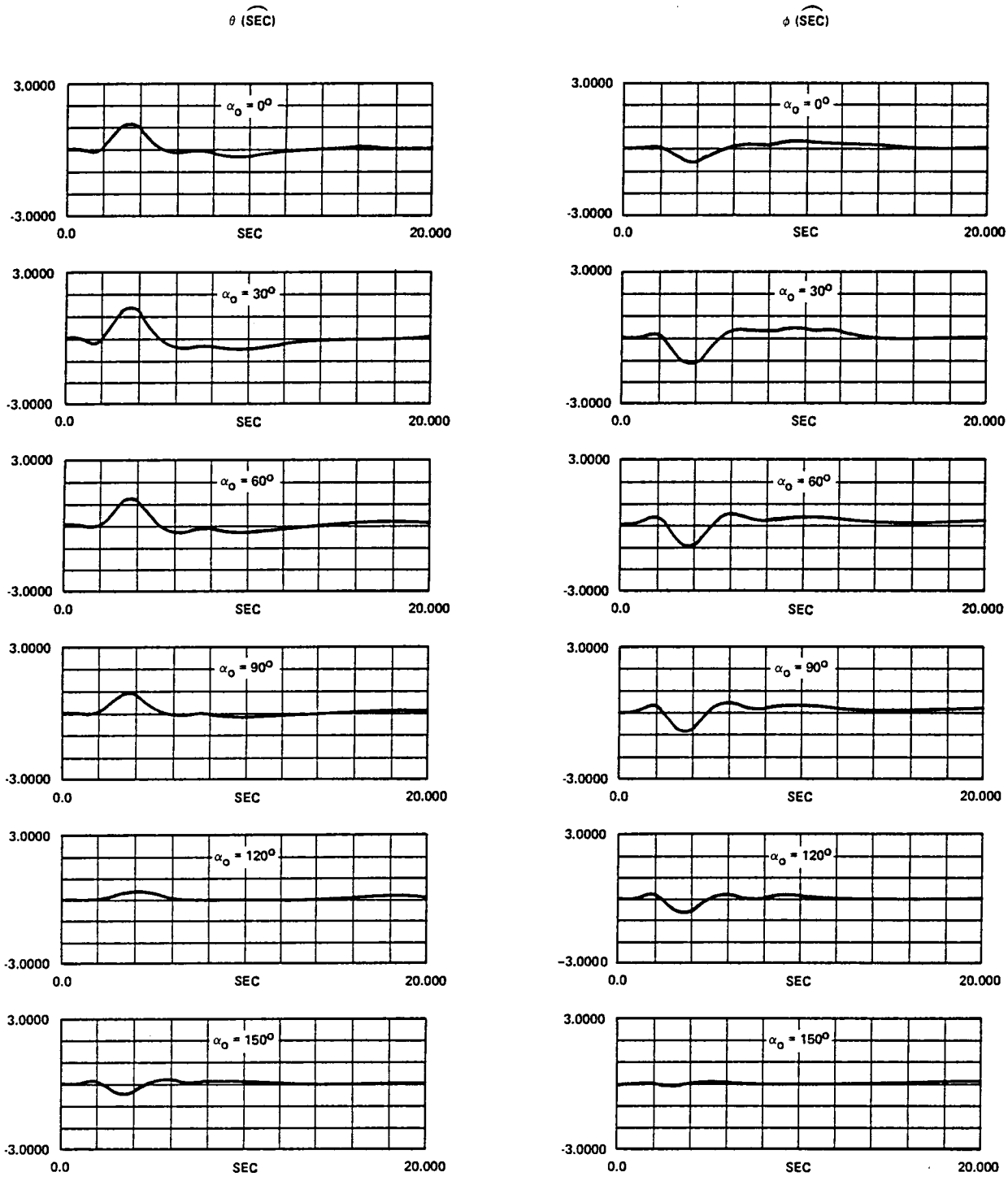

Figure 27
Radial VRCS Data
(Sheet 1 of 2)

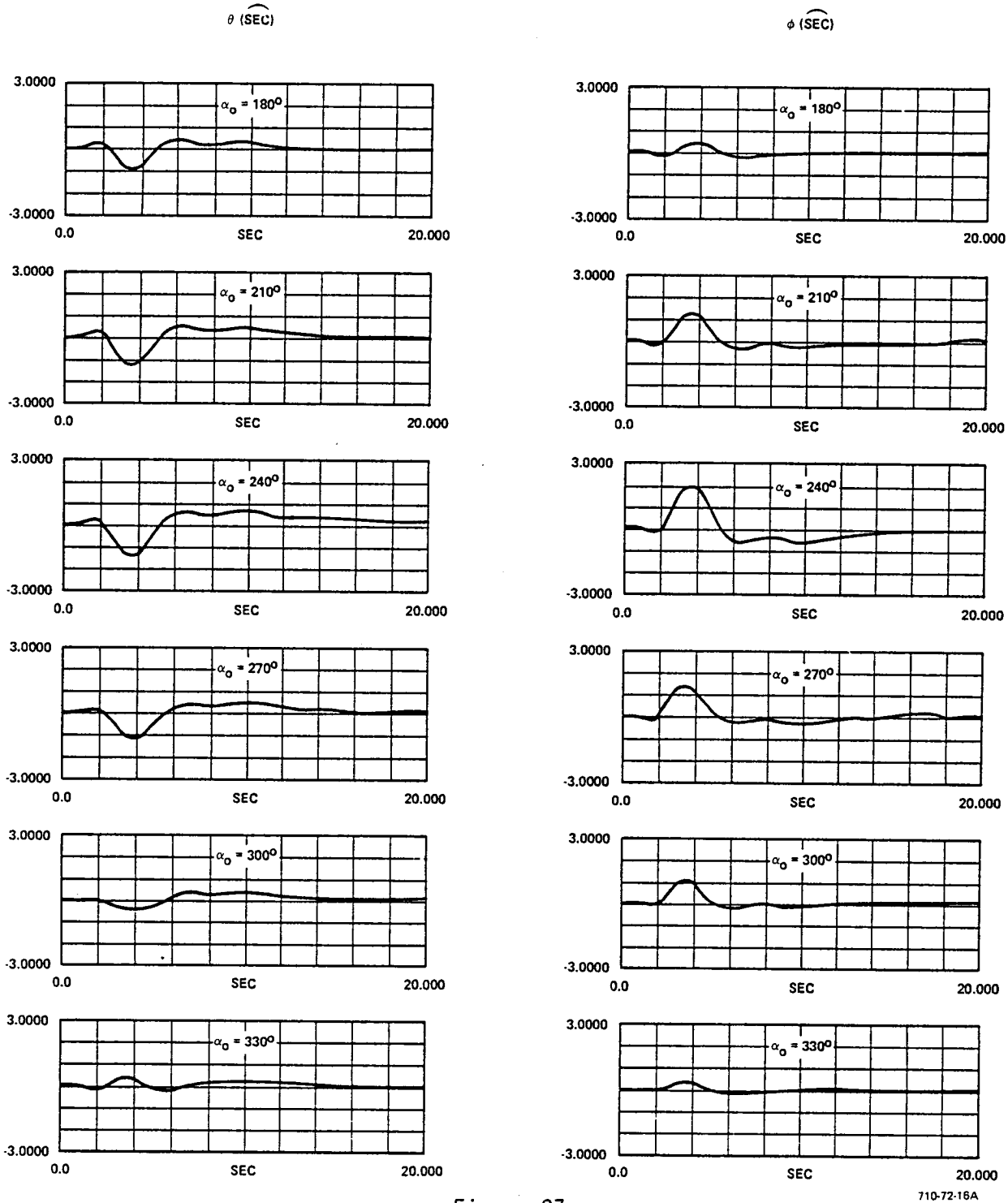

Figure 27
Radial VRCS Data
(Sheet 2 of 2)

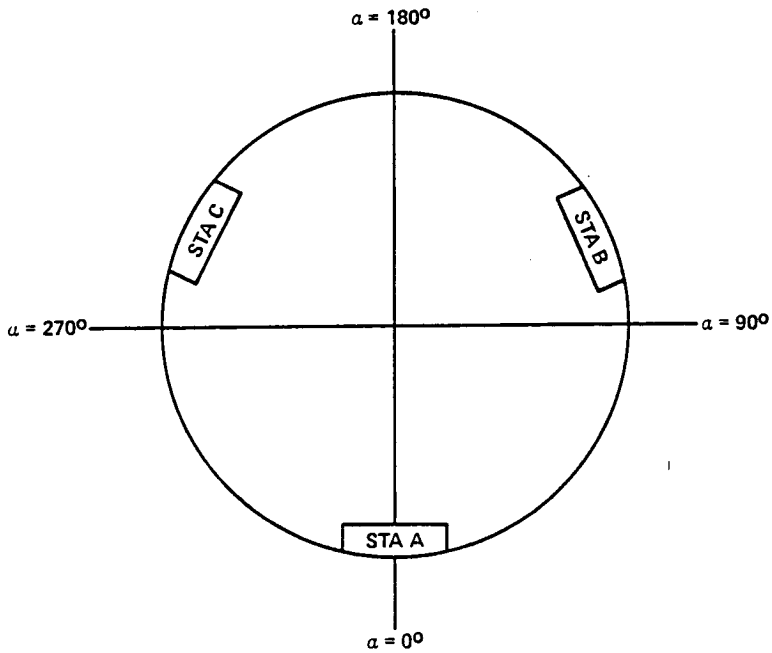

THE DISTURBANCE ANGLE OF ROTATION IS THAT WHICH WOULD RESULT IF THE ROTOR WERE PUSHED INWARD AT A POSITION α^{o} AS ABOVE

EXAMPLE: $\alpha = 0^{o}$ WOULD BE $+\theta$ ROTATION

P5121-40-66

Figure 28
"α" Rotation Angle

α-VALUE OF DISTURBANCE INPUT	PEAK VALUES ($\overline{SEC}$) θ	ϕ	COMBINED PEAK AMPLITUDE ($\overline{SEC}$)
0	+1.15	− .67	1.32
30	+1.42	−1.23	1.91
60	+1.25	−1.05	1.64
90	+ .84	− .91	1.24
120	+ .36	− .71	.80
150	− .48	− .14	.50
180	− .99	+ .48	1.10
210	−1.33	+1.23	1.85
240	−1.53	+1.97	2.49
270	−1.30	+1.43	1.93
300	− .55	+ .96	1.11
330	+ .32	+ .32	.45
			POINTS PLOTTED BELOW

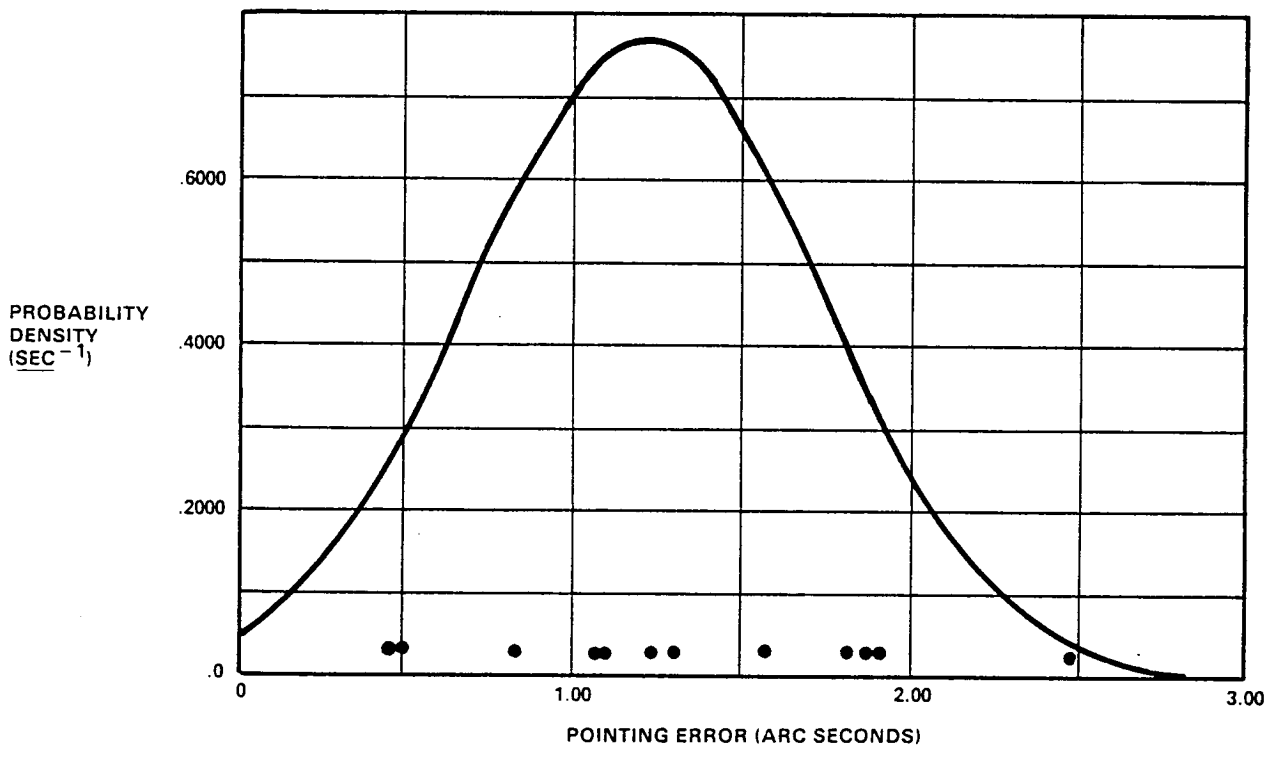

Figure 29
Tabulation of Peak Amplitudes

These values of R are then plotted as points on the X-axis of the probability density curve from Figure 26. Statistically speaking, the mean value of R in the data set is 1.36 arc seconds, compared with 1.22 arc seconds predicted. Similarly, the standard deviation of the data was 0.62 second, compared with 0.52 second predicted. These results are exceptional and say a great deal about the fidelity of the simulation and the accuracy of the system math models.

The Preferred Axis Concept. - In Figure 29, the magnitude of the disturbances which resulted from twelve different cases was tabulated and then plotted as random points on a continuum. Further scrutiny of the data, however, yields a much more interesting method of presentation. In Figure 30, the values of R are plotted as a function of the direction of applied disturbance (alpha coordinate). Note the definitely periodic nature of this curve, indicating that the values of R are not random, but, in fact, are strongly dependent upon the axis of rotation.

This curious phenomenon causes us to ask other questions: for a disturbance at $\alpha = 0°$, why is there so much motion in the ϕ-axis? In fact, at $\alpha = 90°$, why are the magnitudes of θ and ϕ nearly equal?

To study these and other related phenomenon, it is convenient to look at the VRCS disturbance data of Figure 27 in a different coordinate system. Clearly, at any point in time the transverse pointing position can be expressed, not only by θ and ϕ, but also by the amplitude of the rotation, R, expressed in arc seconds and the plane of rotation defined by the alpha coordinate in degrees. Therefore, consider plotting each disturbance, not as θ and ϕ, but as a single plot in the polar coordinates R and α. The same information is conveyed, but in a way which makes clear something which had previously been missed. Figure 31 presents these polar plots for the 12 disturbances. Note the alpha-angles of the actual rotations measured. They all tend to cluster toward +45° or +225° despite the fact that the disturbance force is applied at a different alpha (every 30°) for each plot. Furthermore, when the VRCS disturbance is applied at $\alpha = 45°$ or at $\alpha = 225°$, nearly maximum magnitudes, R, of the disturbances result. Remembering that rotations of 45° and 225° are simply positive and negative disturbances in the same plane, the following becomes a reasonable statement:

> The AVS engineering model has a preferred axis of rotation which corresponds closely to rotation in a plane containing radial bearing U. Disturbances are maximized when in this plane and minimized when 90° away from it. Furthermore, when a disturbance is entered anywhere in between, the payload will twist toward the preferred axis of rotation during the disturbance.

In order to study this twist angle, the values of R and α are tabulated for the peak of each data set in Figure 32. In this table, α_0 is the angle at which the disturbance is applied, and α is the angle of actual rotation of the payload at the time of peak amplitude. The column $\alpha - \alpha_0$, then, is the angle through which the payload twisted in attempting to align itself with the preferred axis. It is interesting, while not surprising, to note that the plots

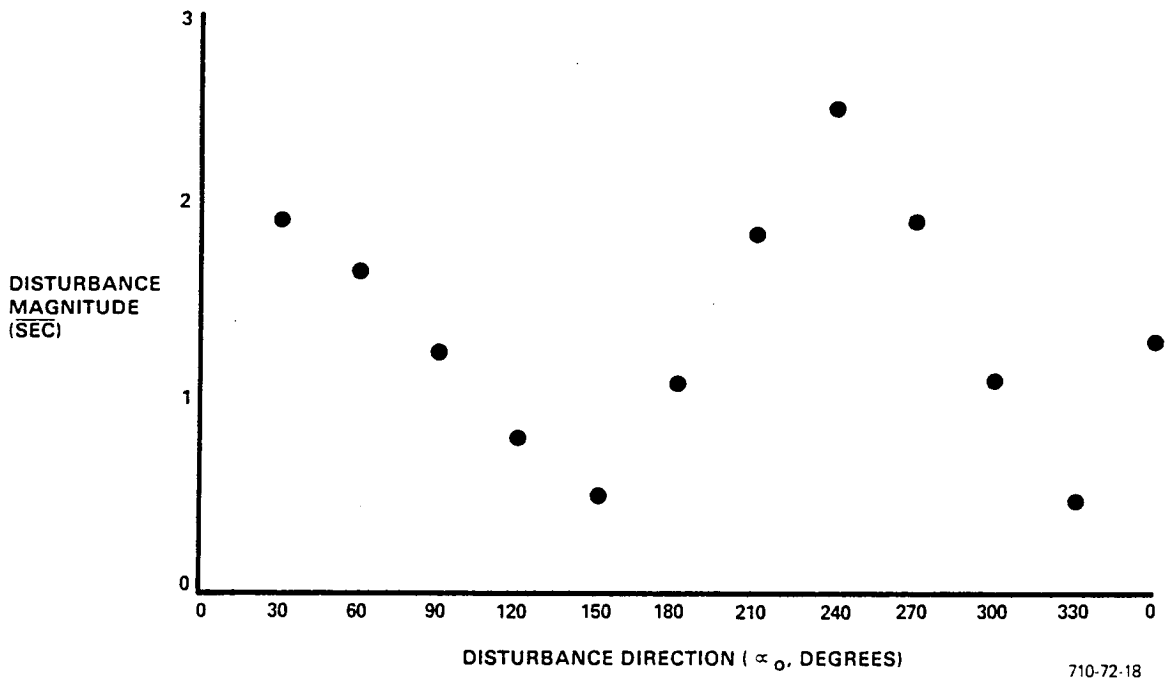

Figure 30
Magnitude Versus Disturbance Angle

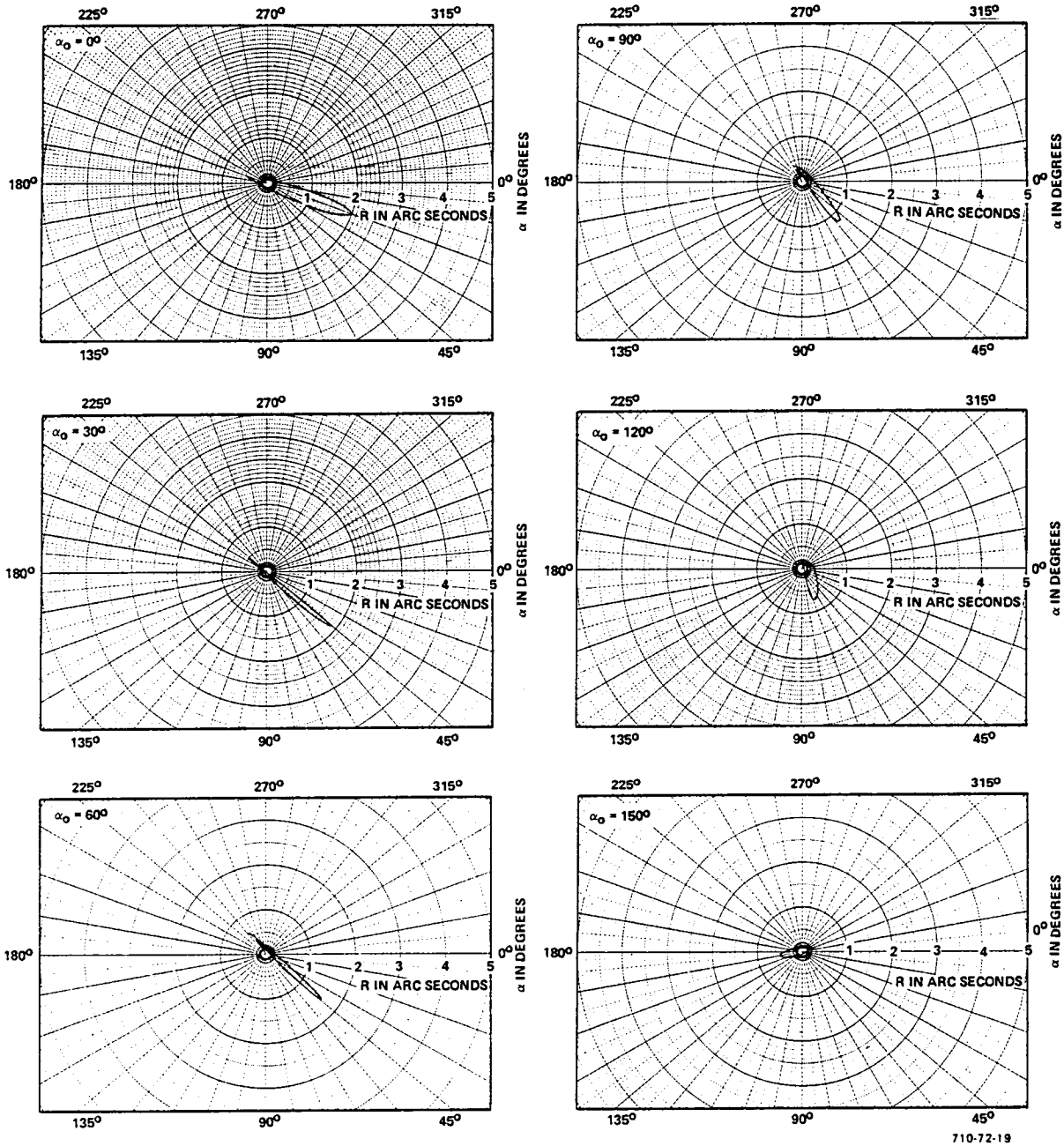

Figure 31
Radial VRCS Data, Polar Plots
(Sheet 1 of 2)

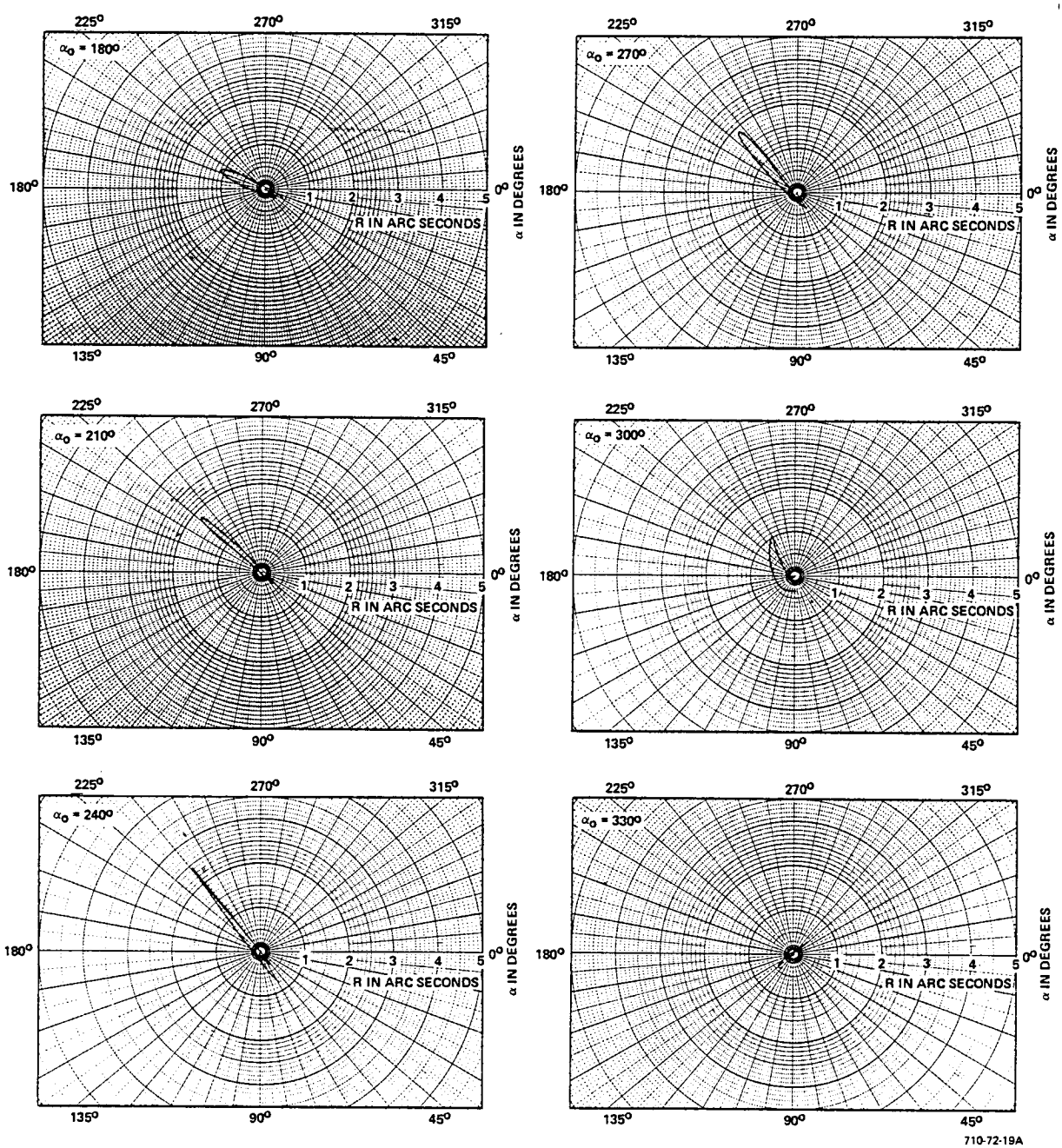

Figure 31
Radial VRCS Data, Polar Plots
(Sheet 2 of 2)

α_o DIRECTION OF DISTURBANCE INPUT	PEAK RESPONSE		COMBINED RESPONSE		
	θ	ϕ	MAG	α	$\alpha-\alpha_o$
0	+1.15	− .67	1.32	30.2	30.2
30	+1.42	−1.23	1.91	41.9	11.9
60	+1.25	−1.05	1.64	40.0	−20.0
90	+ .84	− .91	1.24	47.4	−42.6
120	+ .36	− .71	.80	63.1	−56.9
150	− .48	− .14	.50	164.1	14.1
180	− .99	+ .48	1.10	205.8	25.8
210	−1.33	+1.23	1.85	223.8	13.8
240	−1.53	+1.97	2.49	232.2	− 7.8
270	−1.30	+1.43	1.93	227.8	−42.2
300	− .55	+ .96	1.11	240.4	−59.6
330	+ .32	+ .32	.45	314.6	−15.4

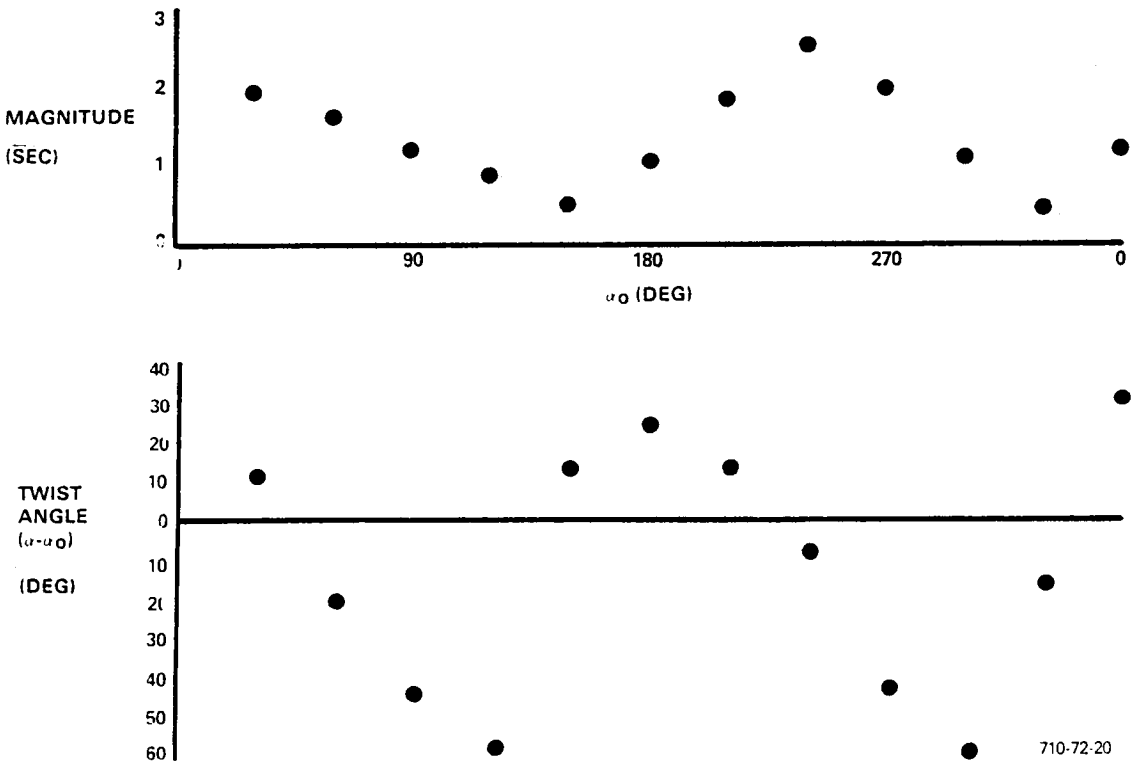

Figure 32
Magnitude and Twist Angle

of (R) and (α - α_0) are roughly in phase quadrature. This is consistent with the qualitative statement above.

Explanation of the Phenomenon: In narrowing down the reason for the preferred-axis behavior, two significant points must be recognized. First, the error is clearly of Type 3 (asymmetric error) since there is a lack of symmetry present. But error sources of Type 3 exist throughout the system and can be the result of asymmetry in either Type 1 or 2. However, in comparing the data of Figure 27 to the plots in Figures 19 and 20, it becomes clear that the predominant error here is of Type 2 due to the shape of the response. Scanning down the list of Type 2 errors, only one is a likely candidate for asymmetry, the gap-related MBA errors. The axial MBAs are rejected immediately since little to no gap motion occurs in these bearings during a radial VRCS. The primary suspect, therefore, is error force in the radial bearings U and V which is a function of U and V gaps and of different slope in the bearings. This is the point at which the data of Figures 24 and 25 were taken to determine if such an error was indeed present. The results were not surprising. A strong gap-gradient exists in the V-bearing which acts like a positive spring and constrains V-axis motion. To say that it is difficult for the base of the payload to move in the plane containing station V is synonomous with saying it prefers to rotate in the plane containing station U, thus the preferred axis. At first glance, one would conclude that the reason for the preferred axis is that station V is out of calibration. It should be emphasized at this point that the difference between the two slopes could be just as large even with the bearings both in specification. In fact, the difference is what causes the preferred axis. If both springs were equal, a large disturbance could exist, but it would be symmetric. This causes one to review the specifications for the bearings, and we are quickly reminded that such problems had been predicted previously and a low bias mode suggested as the solution. The bearings in the laboratory are high bias and are thus subject to greater errors than had been deemed tolerable for fine-pointing. It is then encouraging that the hardware has simply verified this fact.

Justification: In the last section, a possible explanation for the preferred axis was put forward. That explanation will now be justified as correct by both software and hardware. First, in the software, the errors in bearings U and V, as measured, were placed in the math models and the simulation disturbed at several alphas. A plot of the resulting magnitudes of disturbances is shown in Figure 33, along with a copy of the actual hardware data points taken from Figure 32.

As further proof, a spring 46 N/m was artificially added to the engineering model hardware to make the two spring constants equal. When the data were rerun, the preferred axis was almost completely removed as can be seen in Figure 34.

Axial VRCS Disturbance Data. - Statistical predictions for axial pointing stability were not made since this is a special case. The STE should produce no error torques as a function of Z-axis motion and, since the payload CG is nominally on the Z-axis, AVS-produced errors are insignificant, i.e. lateral CG offset is a second-order error source.

A0	THT	PHI	R	A	A-A0
.000	1.473	- .739	1.648	26.634	26.634
30.000	1.642	-1.373	2.140	39.910	0.910
60.000	1.373	-1.642	2.140	50.090	- 9.910
90.000	.739	-1.473	1.648	63.366	-26.634
120.000	.125	- .909	.918	82.187	-37.813
150.000	- .909	.125	.918	187.813	37.813
180.000	-1.473	.739	1.648	206.634	26.634
210.000	-1.642	1.373	2.140	219.910	9.910
240.000	-1.373	1.642	2.140	230.090	- 9.910
270.000	- .739	1.473	1.648	243.366	-26.634
300.000	- .125	.909	.918	262.187	-37.813
330.000	.909	- .125	.918	7.813	37.813

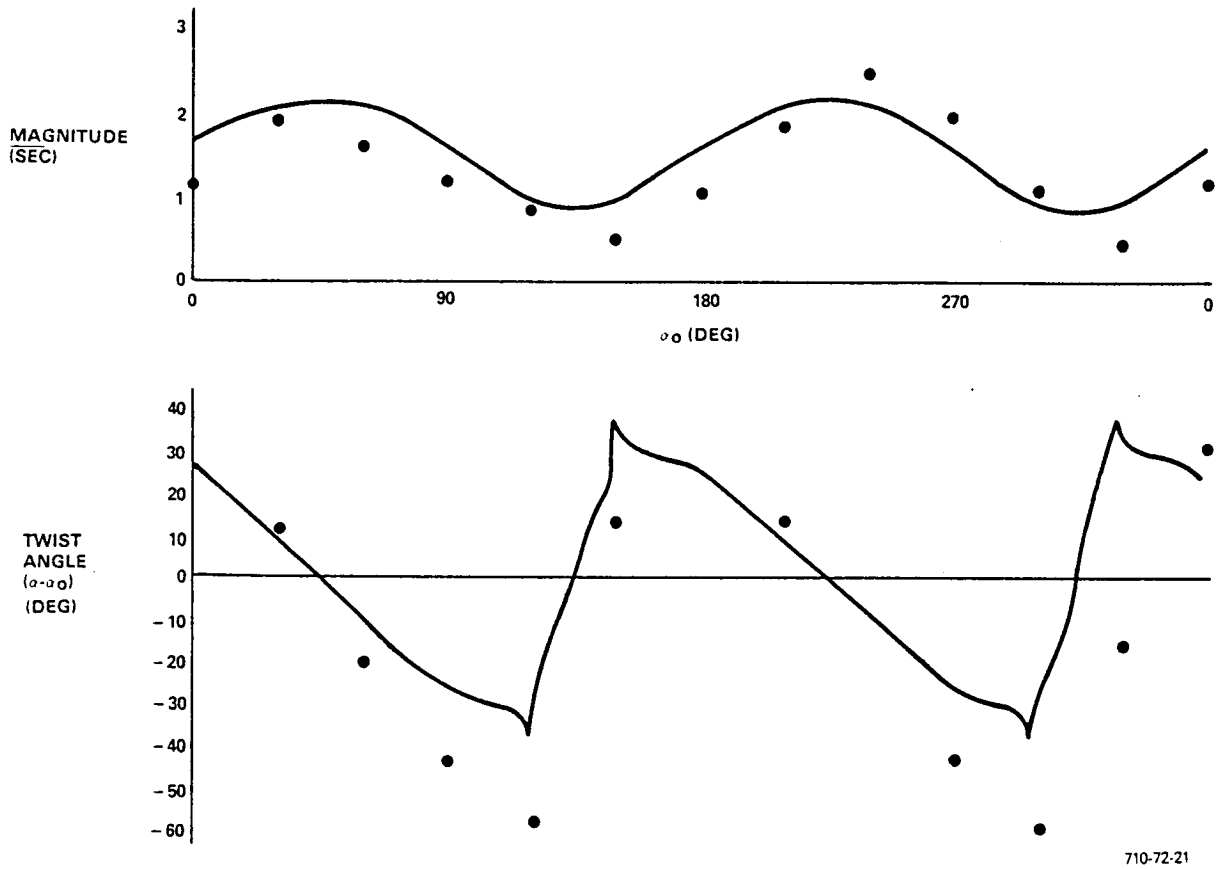

Figure 33
Magnitude and Twist Angle Predicted for
Measured MBA Spring Constant Type 3 Error
(Solid Lines, Prediction; Points, Actual Data)

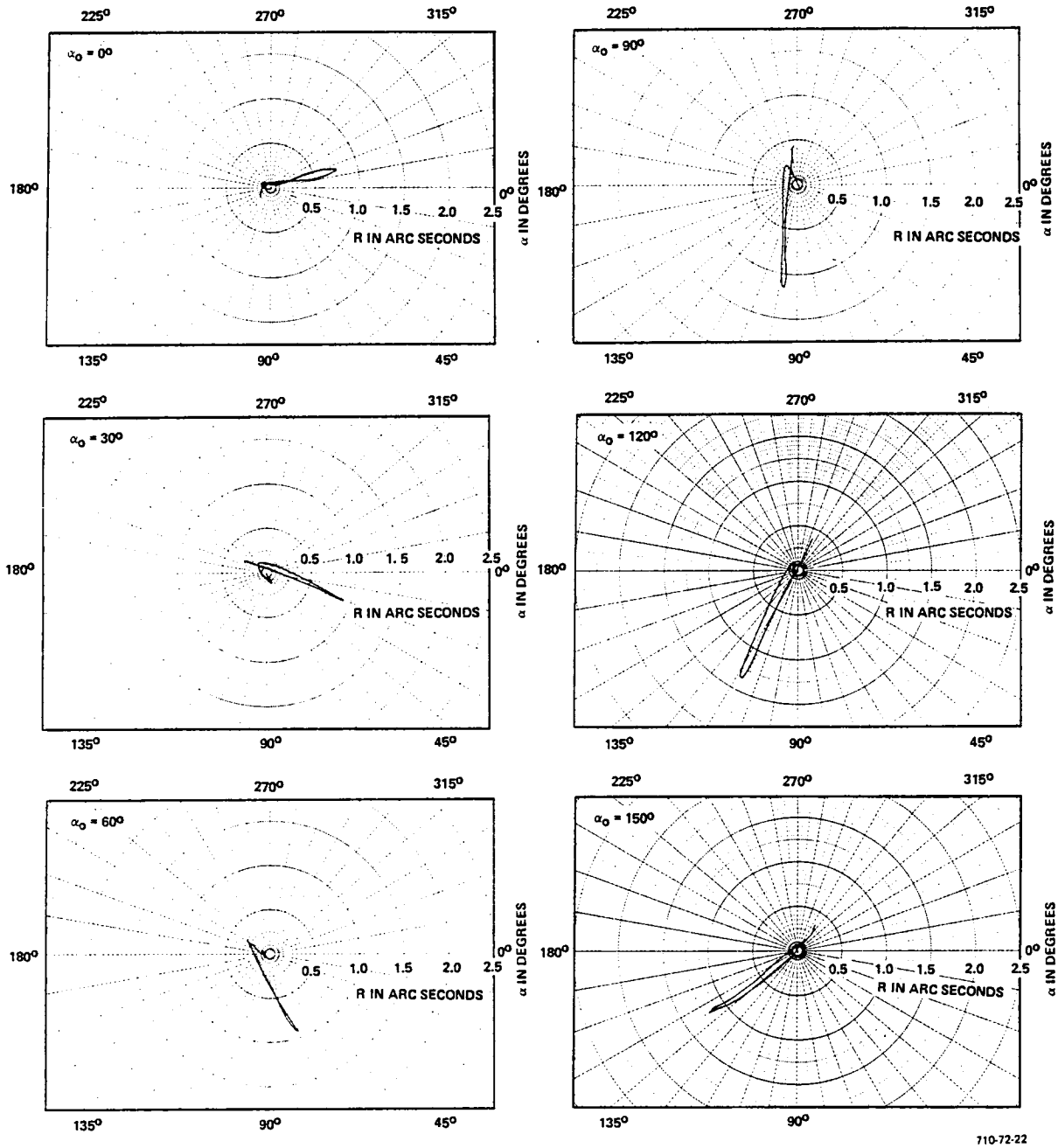

Figure 34
Radial VRCS Data with 46 N/m Added, Polar Plots
(Sheet 1 of 2)

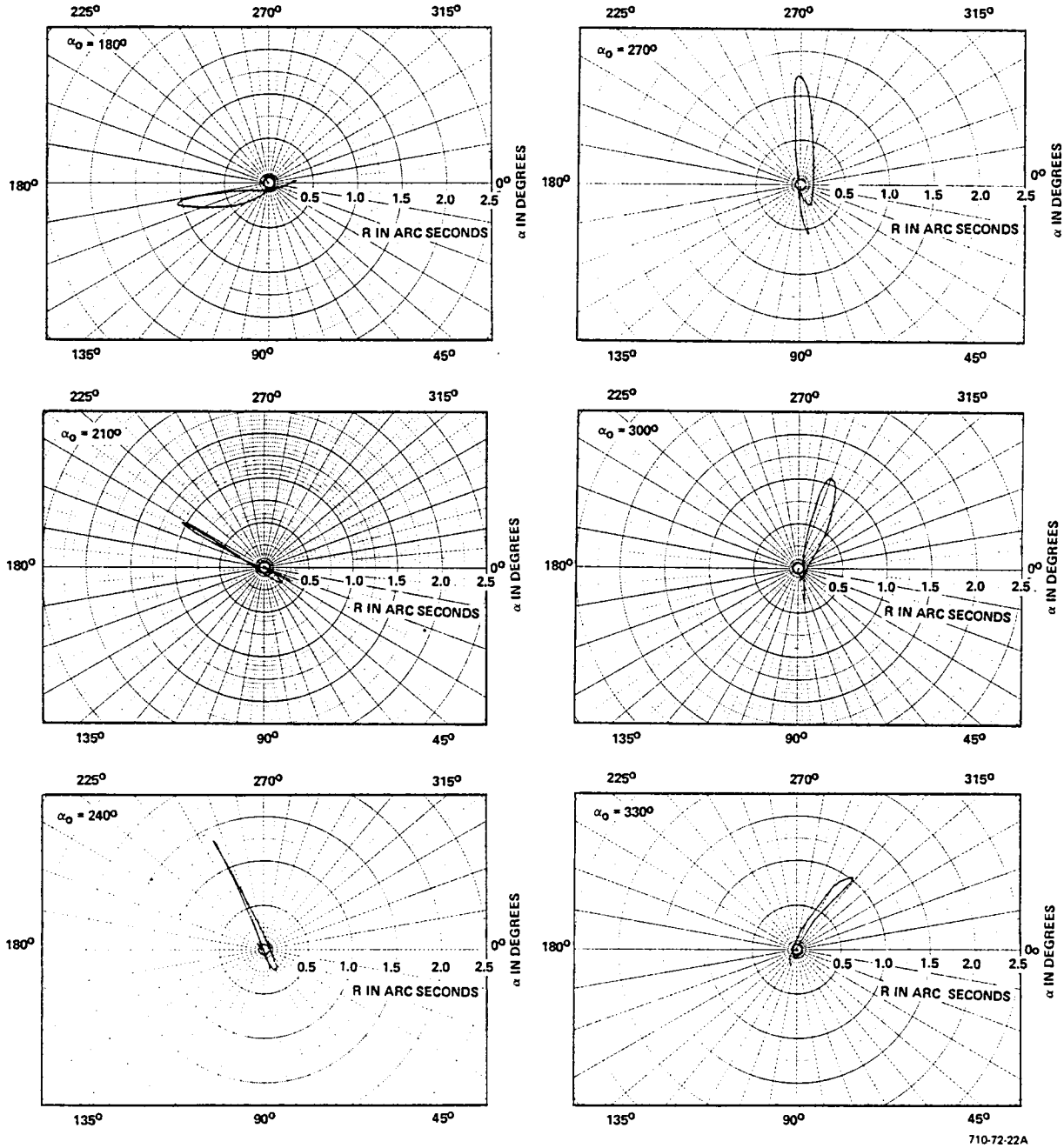

Figure 34
Radial VRCS Data with 46 N/m Added, Polar Plots
(Sheet 2 of 2)

Axial VRCS tests were made using the same disturbance signal as the radial VRCS tests. The data, plotted in Figure 35, clearly shows a significant disturbance. However, this disturbance is of a familiar shape, and the same error source could be prominent here as was the case in the radial VRCS. Tabulating the two runs, we get:

Disturbance	θ (arc sec)	ϕ (arc sec)	R (arc sec)	α (deg)
+Z	-0.508	1.0068	1.13	243
-Z	0.786	-1.329	1.54	59

and the possibility is practically confirmed. The rotation angles, 59 and 243, are within degrees of the plane containing axial station C. Due to the counterbalanced laboratory suspension, it is not possible to measure the axial bearing spring constants. Even so, a very plausible theory is that effective springs also exist in MBAs A, B, and C, and the one in station C has the smallest value; thus the payload rotates in that plane.

Roll Disturbances. - The AVS engineering model is a five-degree-of-freedom system, with the roll axis passively constrained by the torsional stiffness of the suspension cable. Since no control is being exercised on this axis, it exhibits continuous pendulous motion at an amplitude of approximately 10 arc seconds. To verify the lack of coupling to this axis from the other five, a laser measurement of the roll angle was made and monitored during VRCS disturbances like those in the previous sections. Disturbance to the pendulous oscillation was less than 5 percent in all cases.

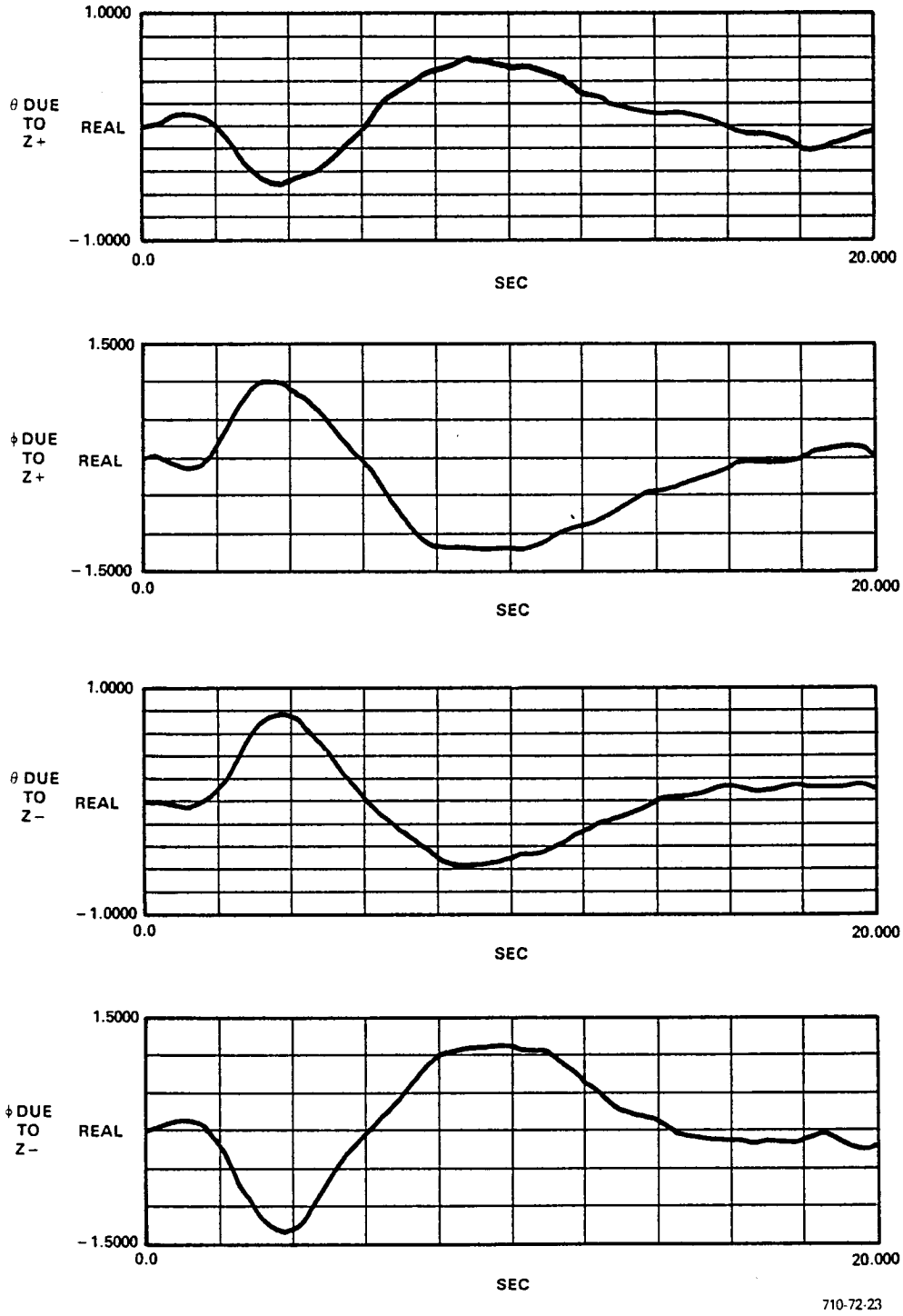

Figure 35
Z-axis Disturbances (arc seconds)

CONCLUSIONS

A protoflight ASPS Vernier System (AVS) has been tested in the laboratory for pointing stability during simulated Shuttle disturbances. The hardware performance was repeatable within the three-sigma analytical predictions. For the worst-case radial VRCS Shuttle disturbance, the predicted and actual peak pointing stability error is as follows:

	Predicted (arc sec)	Actual (arc sec)
Mean	1.22	1.36
Standard Deviation	0.52	0.62

The successful prediction of laboratory test results provides increased confidence in the analytical understanding of the AVS technology and allows confident prediction of in-flight performance. Recently updated computer simulations of ASPS confirm compliance with the specified 0.01-arc second pointing stability design goal while operating in the Shuttle disturbance environment.

No additional technology deficiencies were discovered during these pointing stability tests.

The absolute magnitude of the pointing stability in the laboratory was predicted to be much larger than in flight. The primary contributors to the larger error are:

- Nonideal zero-g payload suspension
- Low bias mode not yet implemented.
- Lead/lag compensation used instead of rate damping.

None of these contributors will exist in flight.

APPENDIX
STATISTICS OF EQUIVALENT MBA SPRINGS

If no knowledge existed regarding the values of the MBA springs, a good model would be a normal distribution with mean zero and 3 = 25.5 N/m, as shown on Page 37. However, these values have been measured in the laboratory and the statistics are thus altered. A distribution will be derived and the true mean and variance determined; then, as an approximation, these values m and ^{2} will be placed in the table as though the distribution were truly normal.

Springs exist at stations U and V with values 9 and 55 N/m, respectively. Thus if a disturbance is entered directly at U, a spring of 9 N/m will be encountered and if the disturbance is entered closer to the plane containing V, a larger spring will be encountered up to a maximum of 55 N/m in the plane of V. This can be generalized by expressing the spring constant as a function of a disturbance angle alpha, as follows:

$$K_{eq} = 32 - 23 \sin (2\alpha) \tag{A1}$$

where alpha is defined to be zero for a disturbance which results in $+\theta$ motion with no decoupling, and positive in the direction towards $-\phi$ motion. What we would like to compute is the probability density of the spring constant, given that the angle of disturbance is random and uniformly distributed from 0 to 360 degrees. First, consider a simple case in which a random variable, X, is uniformly distributed, like alpha, over 0 to 2π, and the function is a simple sine wave. Then

$$f_1(x) = \begin{cases} \frac{1}{2\pi} & 0 \leq x \leq 2\pi \\ 0 & \text{elsewhere} \end{cases} \tag{A2}$$

and $y = \sin x$.

The probability density $f_2(y)$ can be shown using fundamental laws of expectation to be

$$f_2(y) = \frac{1}{\pi\sqrt{1-y^2}} \tag{A3}$$

which has a distribution function of

$$F_2(y) = \frac{1}{2} + \frac{1}{\pi} \sin^{-1} y. \tag{A4}$$

These are plotted below in (a) and (b). Clearly, the mean of this variable is zero. The variance of a random variable is defined as the second central moment, as follows:

$$\sigma 2 = \int_{-\infty}^{\infty} (y-m)2\ f(y)dy$$

$$= \int_{-1}^{1} y2 f2(y)dy$$

$$= \frac{1}{\pi} \int_{-1}^{1} \frac{y2dy}{\sqrt{1-y^2}} \qquad \text{(A5)}$$

$$= \frac{1}{2}$$

Finally, the standard deviation of this random variable is simply:

$$\sigma = \sqrt{\sigma 2} = \frac{1}{\sqrt{2}} = .707 \qquad \text{(A6)}$$

Extrapolating to the case in which the variable's distribution falls between 9 and 55 instead of between -1 and 1, the curve stays the same, and the values of m and σ are as shown below in (c) and (d). As expected, the mean is 32 N/m. The standard deviation for this distribution is 16.3. As an estimate, the same m and σ will be applied as a normal distribution in the performance prediction.

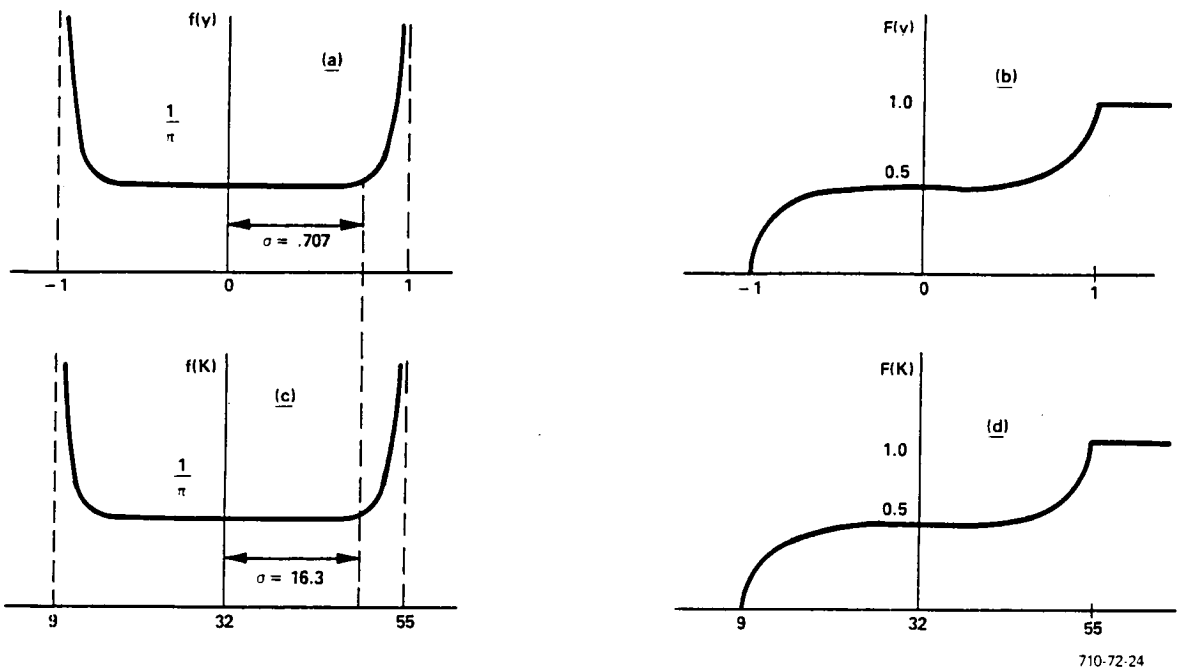

NASA Contractor Report 159307

Distribution List
NAS1-15008

	No. Copies
NASA Langley Research Center Hampton, VA 23665	
Attn: Report and Manuscript Control Office, Mail Stop 180A	1
Anthony Fontana, Mail Stop 152E	30
NASA Ames Research Center Moffett Field, CA 94035	
Attn: Library, Mail Stop 202-3	1
Lou S. Young, Mail Stop 244-13	1
Kenneth R. Lorell, Mail Stop 244-7	1
NASA Dryden Flight Research Center P.O. Box 273 Edwards, CA 93523	
Attn: Library	1
NASA Goddard Space Flight Center Greenbelt, MD 20771	
Attn: Library	1
716.0/Ewald Schmitt	1
717.0/Ken Dolan	1
420.0/Frank Volpe	1
NASA Lyndon B. Johnson Space Center 2101 Webster Seabrook Road Houston, TX 77058	
Attn: JM6/Library	1
NASA Marshall Space Flight Center Marshall Space Flight Center, AL 35812	
Attn: Library, AS61L	1
John H. Owens, JA51	10
Jet Propulsion Laboratory 4800 Oak Grove Drive Pasadena, CA 91103	
Attn: Library, Mail Code 111-113	1
Edward Mettler, Mail Code T-1201	3
Kitaw Ejigu, Mail Code 158-244	1
NASA Lewis Research Center 21000 Brookpark Road Cleveland, OH 44135	
Attn: Library, Mail Stop 60-3	1
NASA John F. Kennedy Space Center Kennedy Space Center, FL 32899	
Attn: Library, NWSI-D	1

	No. Copies
National Aeronautics and Space Administration Washington, DC 20546	
Attn: RS-5/Dell P. Williams III	1
RSI-5/Dr. Joseph Lundholm, Jr.	5
SM-8/Robert A. Kennedy	1
ST-5/Jesse W. Moore	1
RSS-5/Richard F. Carlisle	1
Space Division Worldway Postal Center P. O. Box 92960 Los Angeles, CA 90009	
Attn: YN/Col. B. P. Randolph	1
YND/Lt. Col. H. A. Shelton	1
SAMSO Worldway Postal Center P. O. Box 92960 Los Angeles, CA 90009	
Attn: DYT/Lt. M. Johnson	1
DYT/Major Carl Jung	1
Defense Advanced Research Project Agency 1400 Wilson Boulevard Arlington, VA 22209	
Attn: Lt. Col. Ronald F. Prater	1
Lt. Col. Mel O'Neil	1
Headquarters USAF/AFRDS Washington, DC 20330	
Attn: Maj. Robert R. Wilds	1
NASA Scientific and Technical Information Facility 6571 Elkridge Landing Road Linthicum Heights, MD 21090	26 plus reproducible
Sperry Flight Systems Phoenix, Arizona 85036	
Attn: Brian J. Hamilton (108C)	30

1. Report No.	2. Government Accession No.	3. Recipient's Catalog No.
NASA CR-159307		

4. Title and Subtitle	5. Report Date
Laboratory Evaluation of the Pointing Stability of the ASPS Vernier System	June, 1980
	6. Performing Organization Code

7. Author(s)	8. Performing Organization Report No.
Brian J. Hamilton	5121.5869.6.1-5
	10. Work Unit No.

9. Performing Organization Name and Address	11. Contract or Grant No.
Sperry Flight Systems P. O. Box 21111 Phoenix, Arizona 85036	NAS1-15008
	13. Type of Report and Period Covered
12. Sponsoring Agency Name and Address	Contractor Report
NASA Langley Research Center Hampton, VA 23665	14. Sponsoring Agency Code

15. Supplementary Notes

16. Abstract

The Annular Suspension and Pointing System (ASPS) is an experiment pointing system designed for 0.01 arc second pointing stability in Space Shuttle applications. A protoflight ASPS Vernier System (AVS) is tested in the laboratory. Payload pointing stability is determined in the simulated Shuttle disturbance environment. Statistical predictions of laboratory test performance are compared to actual performance. Analytical understanding of the AVS magnetic bearing technology is demonstrated, allowing confident analytical prediction of in-flight performance.

17. Key Words (Suggested by Author(s))	18. Distribution Statement
Pointing Stability Magnetic Actuators Magnetic Suspension Vibration Isolation	Unclassified-Unlimited

19. Security Classif. (of this report)	20. Security Classif. (of this page)	21. No. of Pages	22. Price*
Unclassified	Unclassified	60	

For sale by the National Technical Information Service, Springfield, Virginia 22161

End of Document